SIMULATION OF NON-LINEAR BENDING BEHAVIOUR OF ULTRA-THIN WOVEN COMPOSITES

V. G. Eroshan Sandeepa Gamage

238045K

Degree of Master of Science

Department of Civil Engineering
Faculty of Engineering

University of Moratuwa
Sri Lanka

April 2025

SIMULATION OF NON-LINEAR BENDING BEHAVIOUR OF ULTRA-THIN WOVEN COMPOSITES

V. G. Eroshan Sandeepa Gamage

238045K

Dissertation submitted in partial fulfilment of the requirements for the degree of Master of Science

Department of Civil Engineering
Faculty of Engineering

University of Moratuwa
Sri Lanka

April 2025

DECLARATION

I declare that this is my own work and this Dissertation does not incorporate without acknowledgement any material previously submitted for a Degree or Diploma in any other University or Institute of higher learning and to the best of my knowledge and belief it does not contain any material previously published or written by another person except where the acknowledgement is made in the text. I retain the right to use this content in whole or part in future works (such as articles or books).

Signature: Date: 04/05/2025

The supervisors should certify the Dissertation with the following declaration.

The above candidate has carried out research for the Degree of Master of Science Dissertation under our supervision. We confirm that the declaration made above by the student is true and correct.

Name of Supervisor: Prof. H. M. Y. C. Mallikarachchi

Signature of the Supervisor: Date: 05/05/2025

Name of Supervisor: Dr. H. M. S. T. Herath

Signature of the Supervisor: Date: 05/05/2025

I would like to dedicate this thesis to my loving parents my sister and all the friends and colleagues who helped me through this journey. . . .

Acknowledgements

First and foremost, I would like to express my heartfelt gratitude to my research supervisors, **Prof. Chinthaka Mallikarachchi** and **Dr. Sumudu Herath**, for providing me with the invaluable opportunity to conduct this research under their expert guidance. Their constant encouragement, insightful advice, and unwavering support motivated me to strive for excellence. This work would not have been possible without their mentorship and dedication.

I would like to extend my sincere thanks to **Prof. Priyan Dias** and **Dr. Lakshitha Fernando** for their valuable feedback and thought-provoking comments during the progress reviews. Their suggestions inspired me to think creatively and approach problems from unique perspectives.

I am deeply grateful to **Dr. Hasitha Wijesooriya** for providing the experimental data, including CT X-ray scans, and for his kind support and guidance during the experimental phases of this work. I also wish to express my sincere thanks to the **California Institute of Technology (Caltech)** and **Prof. Chinthaka Mallikarachchi** for providing the experimental data from the column bending tests, which were conducted by Prof. Mallikarachchi during his time at Caltech. I also gratefully acknowledge **Dr. K. Ubamanyu** for his generous support and guidance throughout the experimental aspects of this research. Their contributions were instrumental to the successful completion of this study.

My special appreciation goes to **Uditha Weerasinghe**, **Lasith Kuruppu**, and **Nisal Ariyasinghe** for their unwavering support, constructive criticism, and engaging discussions, which greatly enriched my research experience.

I also wish to acknowledge the academic staff members of the *Department of Civil Engineering* for their continuous support and encouragement throughout my academic journey.

I am profoundly thankful for the financial support provided by the **National Research Council of Sri Lanka**, which was essential for the successful completion of this research.

Lastly, and most importantly, I extend my deepest gratitude to my family and friends, who have been a constant source of inspiration, strength, and moral support. Their unconditional love and encouragement have been my greatest motivators throughout this journey.

Thank you all for making this endeavor a fulfilling and enriching experience.

Abstract

Ultra-thin woven fibre composites are commonly used to design self-deployable space structures subjected to large deformations. Accurate prediction of their folding and deployment behaviour is crucial for optimising space structures. Recent studies have suggested that in thin woven composites made of one to two layers, the material exhibits a significant reduction in bending stiffness at high curvatures, resulting in a non-linear moment-curvature response, but the phenomenon lacks comprehensive evidence. This study confirms the reported bending stiffness reduction by capturing the complete moment-rotation response from its initial stiffness to failure via a single experimental procedure conducted on coupons. Several approaches are used to construct the bending response from the experimental studies, and their effectiveness is evaluated. The observed experimental response is then captured using a representative unit cell-based homogenised numerical model which is proposed by previous researchers. The model is used to assess the effects of geometrical non-linearities and the material non-linearities of tows on the bending response. The meso-mechanical bending response aligns well with the experimental values. The meso-scale bending response is incorporated into macro-scale simulations via a user-defined section stiffness. Comparison of simulated results with column bending test results obtained through physical experiments shows that the proposed model is capable of accurately predicting the non-linear bending response. The study shows a significant variation in bending stiffness reduction at large curvatures when updating the stiffness matrix in comparison to the simulation performed only with a constant stiffness matrix. Incorporating this change of stiffness is critical for predicting the amount of energy stored for deployment as well as the force required for folding the structure.

Table of contents

List of figures

List of tables

List of Abbreviations

ACS3	Advanced Composite Solar Sail 3
CBT	Column Bending Test
CLT	Classical Lamination Theory
CT	Computed Tomography
DIC	Digital Image Correlation
DSS	Deployable Space Structures
FPB	Four-Point Bending
HSC	High-Strain Composites
LD-FPB	Large Deformation Four-Point Bending
MSAT	Mobile Satellite System
NASA	National Aeronautics and Space Administration
RUC	Representative Unit Cell
SVMBIR	Super Voxel Model-Based Iterative Reconstruction
UTM	Universal Testing Machine
XRCT	X-Ray Computed Tomography

List of Symbols

A Extensional stiffness matrix
B Coupling stiffness matrix
D Bending stiffness matrix
E Young's modulus
G Shear modulus
M Bending moment
N In-plane force resultant
P Applied load
V_f Fiber volume fraction
ε Strain
κ Curvature
ν Poisson's ratio
σ Stress
ϕ Rotation angle
θ Angle
δ Displacement
Δ Difference or increment

Chapter 1

Introduction

1.1 Overview

Recent human attempts on interplanetary and deep space explorations require large space applications which often have dimensions a few times larger than launch vehicles. The concept of deployable space structures came to light in order to accommodate these large applications inside the stringent stowage available in the launch fairings. The concept allows large structures to be compacted into stowage configuration and then expand into operational configuration once delivered. There are many types of deployable mechanisms employed in space structures such as inflatables, shape-memory alloy structures, stored strain energy deployable structures and motorized mechanical hinges.

Among these types, stored strain energy deployable structures made from thin woven fibre composites are self-deployable and do not require additional mechanisms to deploy. This is achieved by folding the structure elastically and releasing the accumulated strain energy for the deployment of the structure. In addition, they have a low mass-to-deployed stiffness ratio, lower costs as a result of fewer components required, and ease of manufacture [2]. Early developments of these applications include Boeing spring-back reflectors on the Mobile SAtellite System (MSAT) [3] and Northrop Grumman Astro Aerospace Flattenable Foldable Tubes (FFT) forming the Mars Advanced Radar for Subsurface and Ionosphere Sounding (MARSIS) antenna on the Mars Express spacecraft [4].

1.2 Woven fibre composites

A composite material is a combination of two or more distinct materials that are engineered to achieve a combination of favourable properties for a certain application compared to individual components alone. Constituents of a composite can be identified by macroscopic level observations. Usually, fibres and the matrix are the two types of constituents that forms a fibre composite. While fibres carry the load, matrix contributes by holding the fibres together and by distributing the loads among the fibres.

Figure 1.1 shows the different types of fibre composites available in the present context. Initially, fibre composites were manufactured using unidirectional fibres embedded in a matrix material. These composites demonstrated significant strength and stiffness along the fibre direction, making them highly suitable for applications requiring high-performance materials with directional properties. However, the lack of strength and stiffness in other directions, coupled with susceptibility to delamination and stress concentrations, limited their use in complex loading conditions [5]. To address these limitations, the development of multi-directional laminates emerged. These laminates combined layers of unidirectional fibres oriented in different directions, improving mechanical properties in multiple axes. Despite these advances, challenges such as interlaminar shear stress, delamination, and difficulty in manufacturing complex geometries persisted.

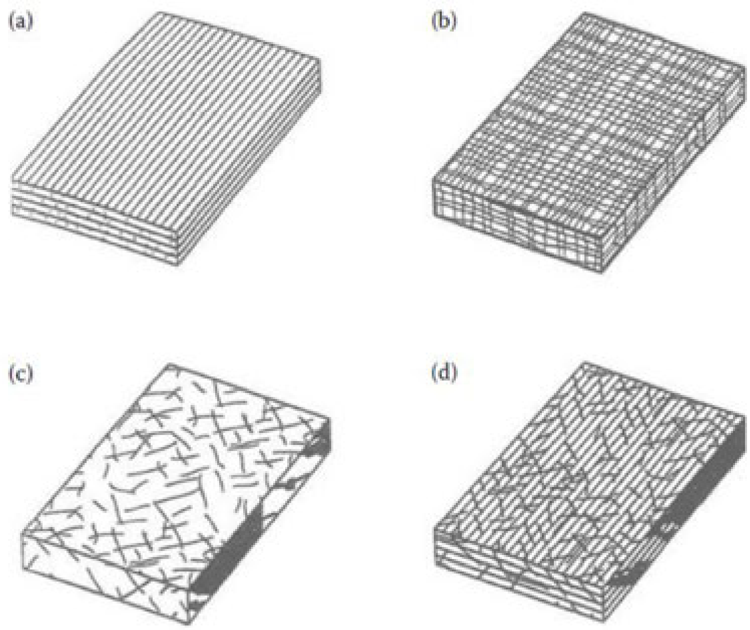

Fig. 1.1 Fibre composite types. (a) Unidirectional fibre composites, (b) Woven composites, (c) Chopped fibre composite, (d) Hybrid composites

The introduction of woven fibre composites represents a significant advancement in composite materials. These composites are made from fibre bundles, known as tows, interlaced in a fabric-like structure. This configuration provides reinforcement in multiple directions within a single ply, enhancing the material's in-plane properties while also significantly improving through-thickness performance. This improvement reduces the risk of delamination, a common issue in conventional laminated composites [6].

Figure 1.2 illustrates woven fibre composites manufactured with various weave patterns, designed for diverse applications in both 2D and 3D configurations.

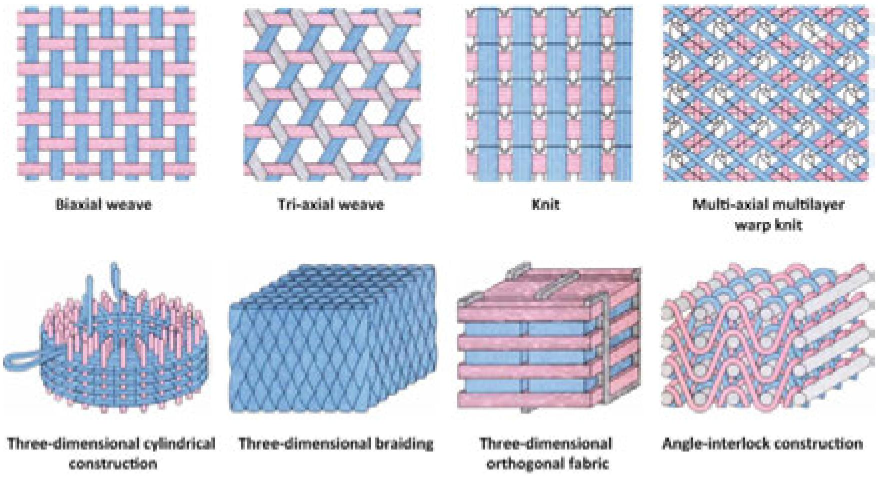

Fig. 1.2 Weave patterns used in woven fibre composite laminates

Thin woven fibre composites have gained considerable popularity due to their exceptional mechanical properties, including high specific stiffness and strength. Additionally, their customizable material and structural performance enable a wide range of innovative design possibilities. Recent advancements in additive manufacturing techniques, such as four-dimensional printing, parametric fibre orientations, and non-developable surface construction, have further expanded the versatility and application potential of woven composites [7]. Moreover, technologies from the textile industry are being ingeniously adapted to produce woven fibre composites with enhanced intra- and inter-laminar strength, as well as superior damage tolerance, far surpassing the capabilities of conventional unidirectional laminates.

The thin sections of woven fibre composites allow for significant bending curvatures prior to failure, offering a flexibility that is particularly advantageous for deployable space structures, where the structures have to be highly compacted for stowage. Since the self-deployability of DSS made of thin woven composites is obtained by bending the structural components elastically to store the energy and subsequently releasing the strain energy at the deployment, most of these structures are subjected to high curvatures during both folding and deployment. For the material to be successfully utilized in and optimized in future structures, accurate mechanical behaviour and failure mechanism predictions are crucial, especially at high curvatures.

1.3 Recent developments and challenges

Self-deployable structures made from thin woven fibre composites are becoming more popular in advanced space missions in order to achieve various mission objectives.Figure1.3 [8] shows the most recent developments where ultra-thin woven fibre composites were being utilized in these applications.

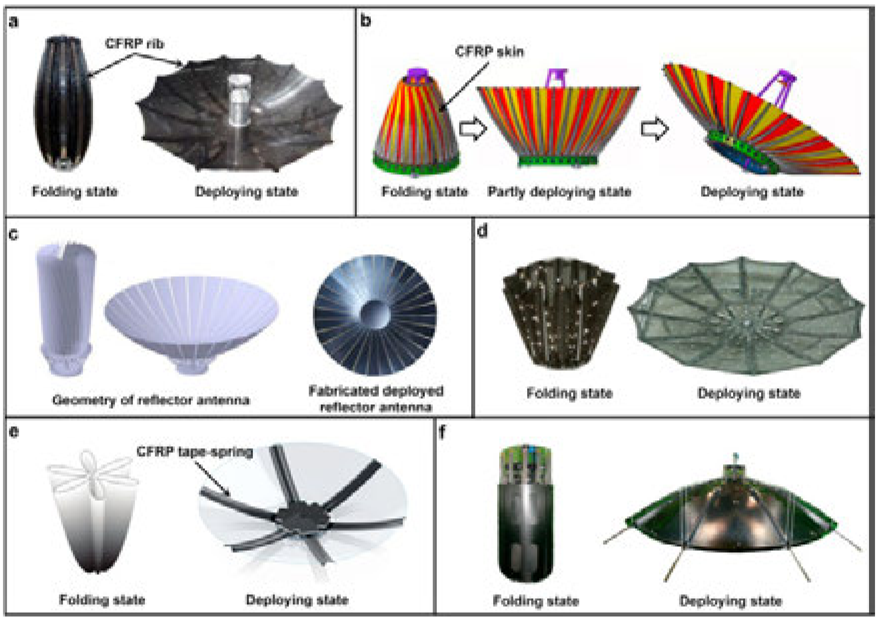

Fig. 1.3 Recent applications of thin woven fibre composite laminates in deployable structures [8]

The supporting structural frame of deployable booms of advanced composite solar sail 3 (ACS3) developed by NASA is a state-of-the-art example which is shown in Figure1.4 [9]. The structural frame is deployed from a small cube-sat which demonstrates the capability of the thin-walled fibre composite booms to achieve the future low-cost deep space mission objectives. The dimensions of the cube sat is around 12 Units (1 Unit = 10 cm × 10 cm × 11.35 cm) while the deployable booms are 7 meters long. Furthermore, it is also evident that they have to be folded into extreme curvatures in order to achieve such packaging efficiency. Figure 1.5 shows a scenario where these structures are folded into such curvatures.

In the present context, the mechanical properties of woven fibre composites under high curvatures are not well understood and most design optimizations are done using trial-and-error experimental procedures. However, these physical experiments are highly expensive, less flexible and time-consuming compared to the predictive models. Anomalies observed during the deployment of MARSIS antenna are a classical example of the need for accurate

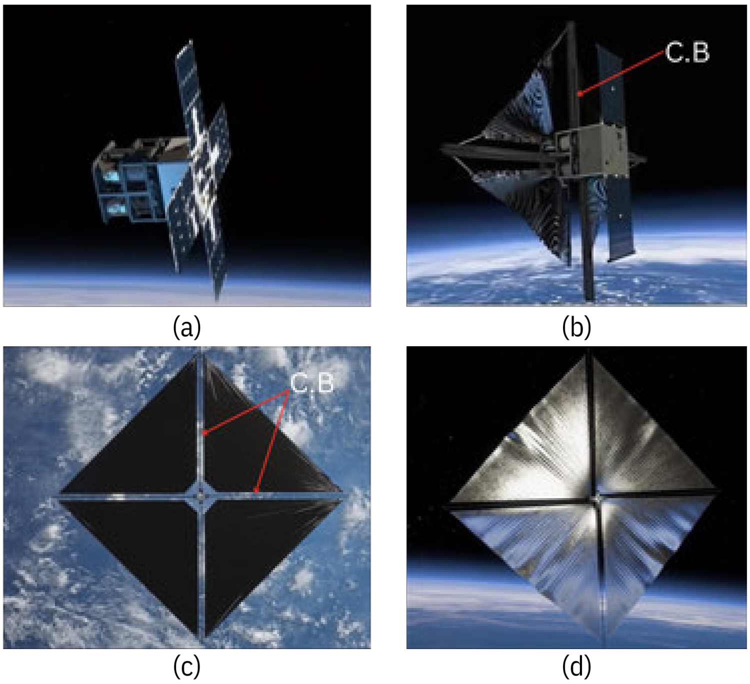

Fig. 1.4 Different stages of deployment of the NASA's ACS3 (CB:Composite boom) [8]

predictive models to understand the mechanical behaviour before the deployment of these structures [4].

Analytical methods such as Classical lamination Theory (CLT) are commonly used to calculate the mechanical properties of composite laminates. Although it predicts both in-plane and out-of-plane properties of woven fibre composites with three or more plies with good accuracy, it overpredicts the bending properties of ultra-thin woven fibre composite laminates by 200% - 400% [10]. This is because CLT does not account for varying thickness and waviness of the laminate which is significant in ultra-thin woven fibre composites.

Fig. 1.5 A composite tape-spring hinge subjected to high curvatures.

As a result, multi-scale modelling techniques have been utilised to predict macroscopic properties of the composite by linking underlying micro-structure through volume averaging of field variables conserving consistency. The necessity of multi-scale modelling arises from the inherently complex nature of micro-scale architecture, which demands high computational resources and yields excessive irrelevant information when all details are included in a single model. Different application-specific hierarchical scales are employed in various analyses, with the most common scales used to analyse woven composites being the micro, meso, and macro scales. Multiple studies using different idealization techniques and different geometrical models have been carried out over the years. Most of these studies focused on capturing initial section stiffness values in the form of ABD stiffness matrix and in-plane deformations. A few research studies have captured the bending behaviour of woven fibre composites with a reasonable accuracy which is a governing factor in aerospace applications [11, 12]. Experimental investigation on two-ply plain weave composites performed by Mallikarachchi and Pellegrino (2013) [13] reported a 20% reduction in bending stiffness near failure curvatures, which shows the necessity for studying the non-linear mechanics under large curvatures.

Research studies by Hamillage and Mallikarachchi (2017) [14], and Jayasekara (2020) [15], well predicted the out-of-plane properties in the linear region (small curvatures). More recently Weerasinghe and Mallikarachchi (2022) [16] captured out-of-plane bending response in the non-linear regime using a non-linear tow material model where the material tangent is varied according to the deformation. While these studies were crucial for the understanding of the mechanical properties of the material, they did not provide elaborated insights into the behaviour of the material in the non-linear regime (large folding curvatures) with experimental validations and physical explanations which is crucial for optimising deployable appendages.

1.4 Scope and aim

As described above, current studies on thin woven fibre composites are mainly focused on predicting the structural response of the material under small curvatures, leading to the assumption of linear section behaviour in macro-scale models. But several experimental and numerical studies by Mallikarachchi and others [14, 15, 13, 16] have shown that there is a non-linear bending response of the material in large curvatures, a phenomenon which has not been fully comprehended.

Therefore, the broad aim of this research is to characterise the non-linear bending behaviour of ultra-thin woven fibre composites in large curvatures using experimental and numerical multi-scale modelling approaches, and then develop a numerical modelling technique to integrate the non-linear section behaviour in macro-scale structural simulations. This work is based on a two-ply plain-woven fibre composite made of T300-1k carbon fibre tows embedded in PMT-F4 epoxy resin. The following objectives are defined to achieve the aim of the study,

1. Analyse the flexural experimental test results to characterise the bending behaviour of the material at large curvatures
2. Analyse the 3D X-ray computed tomographic images of the composite laminate to identify the micro scale geometric properties of the material
3. Numerical analysis of meso-scale representative unit cell model of the material to capture the numerical moment-curvature response
4. Couple the meso-scale bending response with a macro scale structural response of the material using an unparallel computation homogenisation method.

The first step of the study is to analyse flexural experiments to obtain the moment-curvature response of the material up to failure. Unlike previous studies, which used separate tests (such as four-point bending to measure initial stiffness and platen folding to determine failure), this study employs the novel column bending test. This method captures the complete non-linear bending profile of the material in a single experiment. Different analytical techniques will be used to interpret the results, assessing both types of non-linearities associated with the material's flexural behaviour.

The next objective involves performing a micro-scale geometric analysis of the composite. Previous studies relied on micrographs to determine the laminate's geometric properties, such as weave length, tow thickness, tow path, and tow cross-sectional area. However, these 2D micrographs are prone to subjectivity and significant deviations from actual values. In contrast, this study will utilize 3D X-ray computed tomography (3D-XRT) to generate volumetric reconstructions of a representative unit cell. This approach significantly reduces the uncertainties associated with conventional 2D micrographic measurements.

A meso-scale numerical analysis will then be conducted using a previously developed representative unit cell geometry by Weerasinghe and Mallikarachchi [16]. This model incorporates strain-dependent material behaviour in the tows and cohesive interactions between plies to replicate realistic meso-scale material and geometric non-linearities to get an accurate macro-scale bending response. A comparative study will evaluate the significance of tow material non-linearity and cohesive interactions relative to material properties and interactions that are independent of strain values.

Finally, the study will conclude by presenting a novel method to couple the meso-scale mechanical response of the material with the macro scale kinematics, which is a crucial aspect of optimising deployable boom structures in real-world applications. This will be achieved by an unparalleled computational homogenization considering the computational cost-effectiveness of the methodology. The column bending test is simulated with a non-linear section response obtained by the meso scale numerical modelling in this final step.

1.5 Chapter organisation

This thesis is organised into six chapters. Chapter 1 introduces woven fibre composites and explains the motivation behind the study. Chapter 2 reviews the existing literature on experimental investigations, flexural testing methods applicable to woven fibre composites, theories behind constitutive relationships, meso-mechanical modelling approaches, and prior studies on the non-linear flexural behaviour of woven fibre composites.

Chapter 3 details the flexural testing experiments conducted on the material and their analysis using three distinct approaches: a geometric closed-form solution, Euler's Elastica solution as analytical methods, and direct Digital Image Correlation (DIC) readings as a baseline method for constructing the bending response. Chapter 4 outlines the multi-scale numerical modelling methodology employed to simulate the bending behaviour of the material at large curvatures. It begins with a micro-scale geometric analysis using 3D X-ray Computed Tomography (3D-XRCT) images and micro-scale tow property homogenisation. It then describes the development of meso-mechanical models for the Representative Unit Cell (RUC) using the finite element software Abaqus/Standard. The chapter further discusses both linear and non-linear analyses conducted with the meso-model and concludes with the macro-scale structural simulation of the laminate incorporating non-linear section properties.

Chapter 5 presents the results from the multi-scale numerical modelling approach and compares them with experimental data. Finally, Chapter 6 concludes the thesis with a summary of findings, and recommendations for future work.

Chapter 2

Literature Review

This chapter discusses the state of the art in ultra-thin composite deployable booms and the criticality of comprehending the material's mechanical properties when optimising the applications. Then, the chapter elaborates on recent experimental, analytical, and numerical studies conducted on thin woven composites to characterise their mechanical properties.

2.1 Stored-strain energy deployable booms

Deployable boom mechanisms made from thin woven fibre composites have been prominently used in the aerospace industry overtaking their counterparts mainly due to two reasons. Firstly, deployable booms made from thin woven laminates store strain energy during the elastic folding step and subsequently use that energy to self-deploy the structure which avoids the need for mechanical hinges, motors and actuators thus making these structures self-reliable. Secondly, these structures are extremely lightweight compared to the other deployable systems which is a crucial factor for cheap and sustainable space missions. Astromesh shown in the Figure 2.1 by Northrop Grumman is an example of a conventional deployable mechanism with mechanical hinges and actuators which is a few times heavier and complex compared to a self-deployable composite boom structure. Therefore, the importance of thin woven composite as a material for high-precision large space systems is evident.

Different criteria can be used to categorise deployable booms. They can be classified based on their purpose and physical characteristics, such as thin-walled tubular booms, telescopic masts, coilable masts, and articulated trusses [17, 18]. The deployment methodology for each category varies depending on the application.

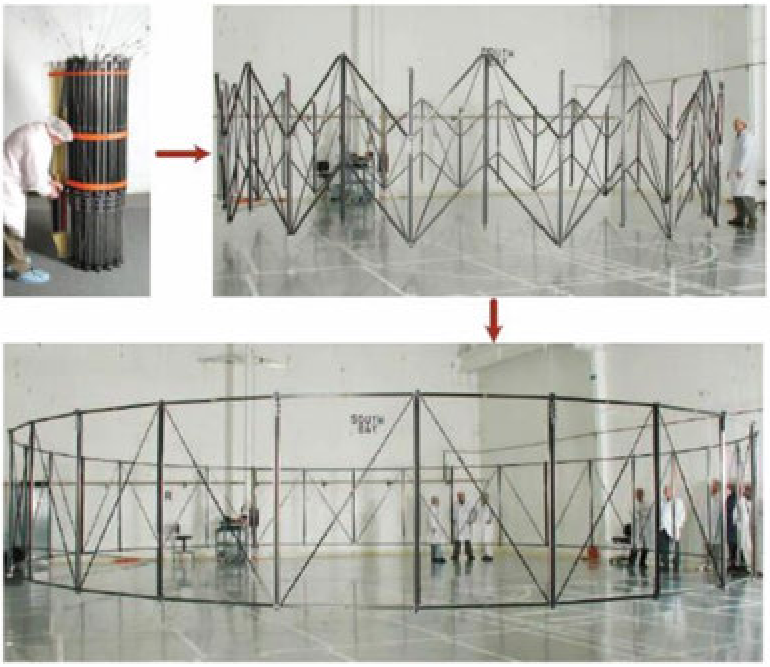

Fig. 2.1 Astromesh 2 by Northrop Grumman (Courtesy: Astro Aerospace)

2.2 Tape spring hinges

The concept of the tape spring hinge comes from the simple mechanism of carpenters' tape. In the aerospace industry, instead of metal alloys, these thin-shell hinge designs are typically made from woven fibre composites due to their high strength-to-stiffness ratio, lightweightness and tailorable properties. One can simply employ a tape spring hinge to deploy a structure without any additional mechanical parts, hence providing a favourable choice as a deployable mechanism. These thin-walled shell structures can endure significant curvatures during their folding and deployment, resulting in elevated stress levels. Slotted hole hinges with varied geometries function as tape springs, enabling large curvatures and stress accommodation. An example of such a hinge is the flattenable foldable boom hinge [19].

In more advanced designs, slotted holes have been replaced with softer matrix materials in hinge regions as shown in the Figure 2.2, creating dual-matrix composite structures capable of withstanding significant curvatures [20]. This innovation led to the development of dual-matrix composite booms, offering self-deployable properties with closed cross-sectional designs.

The deployment behaviour of tape spring hinges can be characterised by observing the moment-rotation envelope, which is typically linear for small angles, as noted by

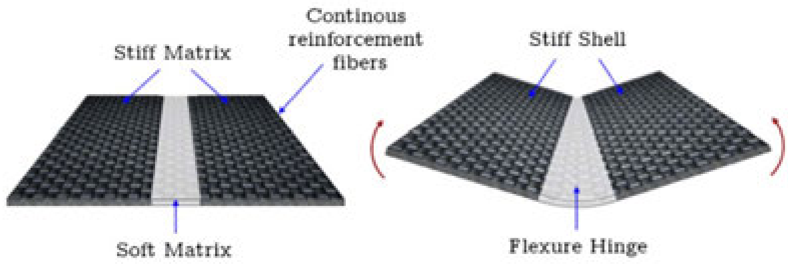

Fig. 2.2 Dual matrix composite hinge

Mallikarachchi [21]. Over the years, numerous numerical studies have been conducted to capture the physical folding-deployment behaviour of these boom structures.

Figure 2.3 illustrates Mallikarachchi's [21] attempt to simulate the quasi-static deployment behaviour of a tape spring hinge made of a two-ply plain woven fibre composite. The simulation incorporated a modified bending stiffness parameter to account for variations in bending stiffness. While the simulation successfully captured the overall deployment behaviour compared to the experiment, it did not accurately reproduce the region between 20° and 0°.

Similarly, Ubamanyu [22] investigated the quasi-static deployment behaviour of a dual-matrix composite boom. Dual-matrix composites feature a softer matrix in the hinge areas and a stiffer matrix in the rest of the laminate. To model this, the bending stiffness was reduced by varying percentages, up to 100%. The study's outcomes were compared with experimental results from Sakovsky [20], revealing that the bending moment varied with the applied curvature.

2.3 Experimental investigations

There have been a number of studies to understand the mechanical behaviour and potential applications of thin woven fibre composites over the recent past. This section reviews the observations and techniques, results and shortcomings associated with those experiments.

2.4 Flexural testing

Ultra-thin woven fibre composites belong to a class of fibre composite materials called high-strain composites (HSC), designed to operate at strains greater than 1 % in bending [23]. When used in strain energy deployables, their primary mode of deformation is bending. Therefore, measuring their bending response is essential for several deployable structural

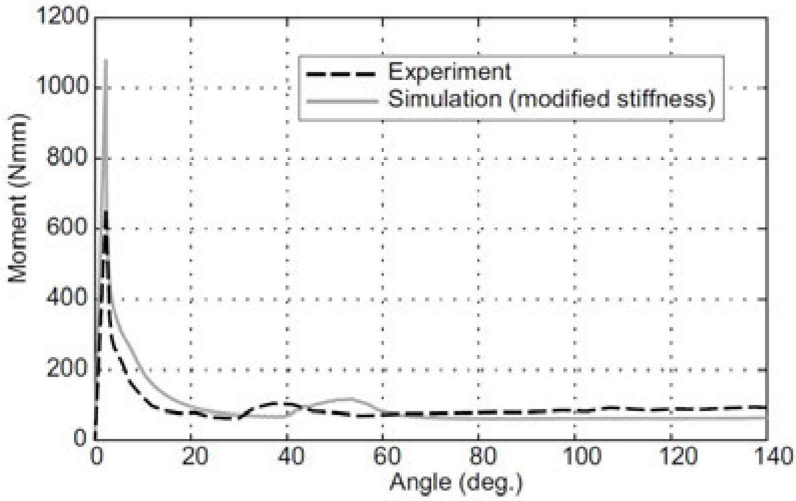

Fig. 2.3 Moment-rotation variation of the tape spring hinge obtained from the simulations and the experiment

designs. Ideally, the bending response of a material should be derivable from the constitutive data obtained from a few simple mechanical tests. However, the microstructural heterogeneity and geometrical complexity of thin woven fibre composites result in complex anisotropic behaviour, exhibiting different tensile, flexural, torsional, and shear mechanical characteristics [24]. Consequently, directly measuring the moment-curvature response of thin woven composites is important, rather than inferring bending properties from tensile and compressive data.

In 2011, Mallikarachchi [21] conducted a series of experiments on a two-ply T300-1k Hexcel 913 plain weave laminate to determine the mechanical properties of ultra-thin woven fibre composites. Tensile, compression, shear, bending, twisting, and biaxial tests were performed in this study. For the bending tests, a four-point bending test was employed, Figure 2.4. The four-point bending test produces a consistent bending moment between the two loading points in the central region, which is not achievable with a three-point bending test. The initial bending stiffness was characterised by taking the mean and standard deviation of 10 trials, considering both loading and unloading. The mean bending stiffness obtained was 37.55 Nmm, with a standard deviation of ±5.54 Nmm. However, due to the thinness, and the geometric and material non-linearities, ultra-thin woven laminates can withstand curvatures of up to 0.3 mm^{-1} before failure. As such, four-point or three-point bending tests are only valid for geometrically linear bending responses and cannot accommodate or characterise large elastic deformations in thin composites, although they are well-suited for thicker counterparts. Consequently, several special-purpose experiments have been designed

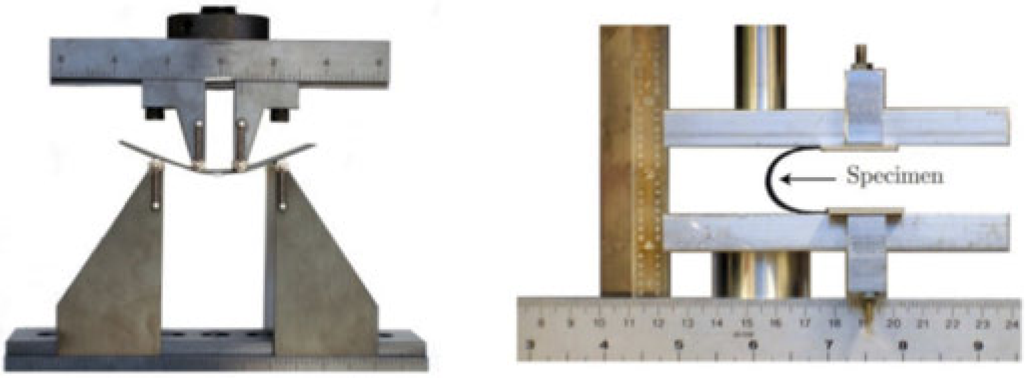

Fig. 2.4 (a) Four point bending test (b) Platen folding test

to test the pure bending of HSCs at large deformations under realistic loading and boundary conditions.

Initial efforts began with the Platen folding test by Yee and Pellegrino in 2017 [25], which can accommodate large deformations up to the failure point of the laminate, Figure 2.4. The platen folding test can accommodate high curvatures in the test coupon but it has several shortcomings as well. Due to the test geometry, a highly localized curvature will be generated at the mid-depth of the coupon and the distribution of the curvature along the coupon is not uniform. To achieve statistically accurate failure curvatures, the material volume portion subjected to the high curvature should be large compared with the rest of the specimen. This condition is not met in the platen folding test hence it gives unrealistic high failure curvatures on some occasions. Mallikarachchi and Pellegrino [21] utilised the Platen folding test to determine the failure point of the two-ply plain woven fibre composite. Seven samples were tested, and failure was observed at $0.203 \pm 0.01\,\mathrm{mm}^{-1}$, with a failure moment of 5.068 ± 0.293 Nmm/mm. However, the extrapolated bending stiffness from their four-point bending experiment gave a moment of 7.623 Nmm/mm at the same curvature. This difference highlights two key facts: first, there is a reduction in bending stiffness with increasing curvature in ultra-thin woven fibre composites, leading to a non-linear bending response; second, the optimisation of deployable structures made from ultra-thin woven fibre composites cannot rely solely on the material's initial bending stiffness. This underscores the need to observe the complete bending response of the material using a single experiment.

As an alternative to the platen folding test and the conventional four-point bending (FPB) test, the large deformation four-point bending (LDFPB) test [26] was developed to characterise the bending response of HSCs. This test is a modified version of the conventional

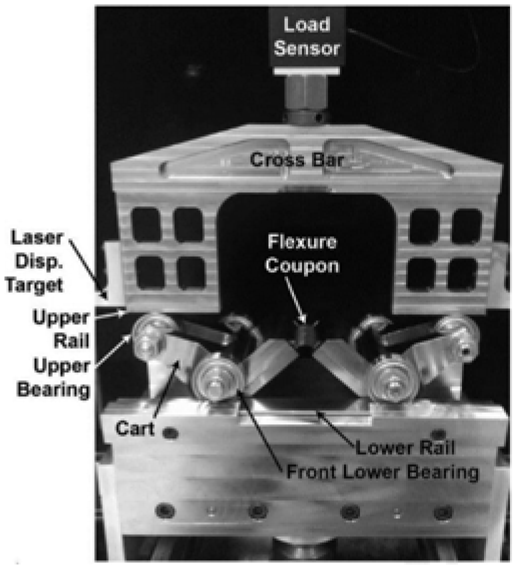

Fig. 2.5 Large Deformation Four Point Bending Test (LD-FPB)

FPB, as shown in Figure 2.5. Like the FPB test, it generates a pure bending stress state in the specimen.

However, the LDFPB test has a more complex configuration compared to the conventional FPB. The ends of the specimen are clamped to carts within the test setup, while the load is applied to a crossbar. As the crossbar moves downward, the carts—supported by bearings—move along the upper and lower rails, causing the specimen to bend while moving upward.

Despite its advantages, the LDFPB test has several shortcomings. One major issue is the frequent failure of the specimen at the clamped locations due to strain localisation. As a result, failure can occur at the steel grips before reaching the mid-section of the specimen, making the results unreliable. Some researchers have used the LDFPB test to evaluate nonlinearities in the bending response of high-strain composites. However, to accurately capture the failure point of the material, conventional platen folding tests were employed instead [27]. Additionally, recent studies have applied the LDFPB test to assess the bending stiffness of thin composite tape-spring designs made from carbon and glass fibres [28].

Another alternative method is the simple vertical test [29]. In this method, the specimen is rigidly attached to steel grips at both the top and bottom. Instead of metal hinges, the outer faces of these grips are connected to the loading head using tapes, which act as hinges. The stiffness of the tapes is considered negligible since their bending rigidity is significantly lower than that of the tested laminate [30].

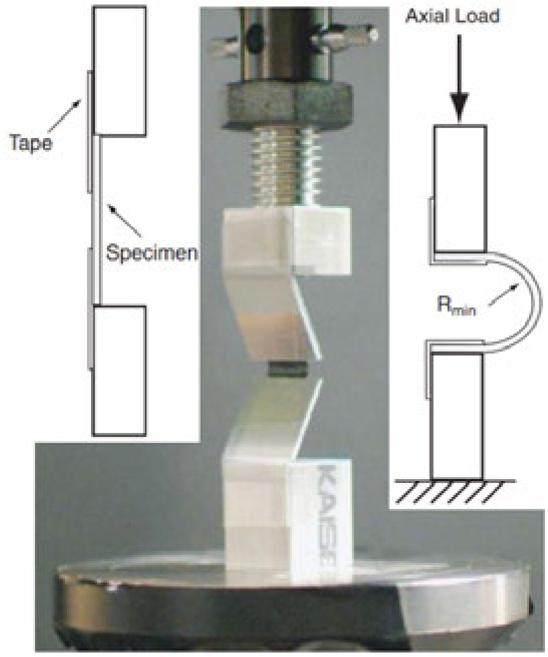

Fig. 2.6 Simple Vertical Test

During the test, the specimen is subjected to compressive loads. When a compressive load is applied using a universal testing machine (UTM), the grips rotate around the taped hinges, causing the specimen to bend. The moment-curvature relationship is then derived from the buckling behaviour of the specimen, as illustrated in Figure 2.6.

However, the vertical test is susceptible to gravity-induced shear deformations at large rotation angles. Because the grips are not balanced around their axis of rotation, they tend to exhibit different rotation angles at the top and bottom locations. This imbalance generates an unbalanced rotational moment in the specimen, leading to errors in the analysis.

The most recent development, the Column Bending Test (CBT) [31, 1, 32, 33], has emerged as the preferred method for testing the full non-linear bending behaviour of thin woven fibre composites up to failure, overcoming the limitations of previous methods by combining beneficial characteristics of both platen folding test and the LDFPB test. The method imitates the case of a column in axially compressed loading and has been employed on several occasions by NASA to characterise high-strain fibre composites. These high-strain composites are used in the new generation of cube sats that uses composite deployable booms. [34–37]

Figure 2.7 illustrates the test setup for the CBT. While the most common CBT configuration is vertically mounted to a universal testing machine (UTM), horizontal configurations are also possible using displacement-controlled loading mechanisms [31]. In the test setup, two rigid arms clamp the specimen at both the top and bottom ends using screws. These arms are then affixed to U-shaped clevises at each end via pinned connections, which are mounted on bearings to minimize friction effects. The pinned connections are deliberately offset from the specimen to induce bending in the desired direction. As the loading head moves downward, the rigid arms rotate within the clevises while simultaneously displacing downward, causing the specimen to buckle.

The CBT replicate a pure bending scenario, inducing failure near the centre of the coupon with a near-uniform moment and curvature within the specimen. This allows the test to be analysed using a simple geometric approach. However, in some cases, significant curvature variations within the coupon can occur, and the simplification may not hold depending on factors such as specimen thickness and fixture arm size [33].

The forces measured during the CBT are relatively small, so reducing gravity-induced forces and moments is crucial for obtaining accurate measurements. Typically, CBT experimental designs follow two approaches: the weight-unbalanced CBT configuration and the counterweight-balanced CBT (CWB-CBT) configuration [31, 38]. Fernandez et al. [31] analysed the gravity effects on weight-unbalanced test configurations and found that gravity-induced moments cause the fixture arms to sag at large rotation angles. They conducted a parametric analysis to quantify the impact of various experimental parameters, such as fixture arm weight, fixture arm length, and coupon free length, on the gravity-induced shear forces and moments on the coupon. The analysis revealed that errors increase with fixture arm weight and length but decrease with coupon gauge length (i.e. thinner coupons requiring shorter gauge lengths for failure during bending tests are more prone to gravity-loading effects than thicker coupons). The CWB-CBT, developed by Opterus R&D, accurately tests thinner laminates requiring shorter gauge lengths by preventing the detrimental effects of gravity-induced errors. The CWB-CBT is symmetrical about the loading pin axis, so the fixture arm's centre of mass coincides with the load application point at the pin, eliminating gravity-induced shear forces and moments. This allows for the direct conversion of universal testing machine data into curvature-moment relationships.

2.5 Multi-scale modelling approach

Multi-scale modelling is a powerful methodology that utilizes models at different scales simultaneously to explain and predict the behaviour of a complex system. This approach has proven to be an effective tool for reducing the need for extensive experimental testing, thereby streamlining the design process and significantly cutting costs [39]. In the context of deployable booms, their behaviour can be analysed across multiple length scales, typically

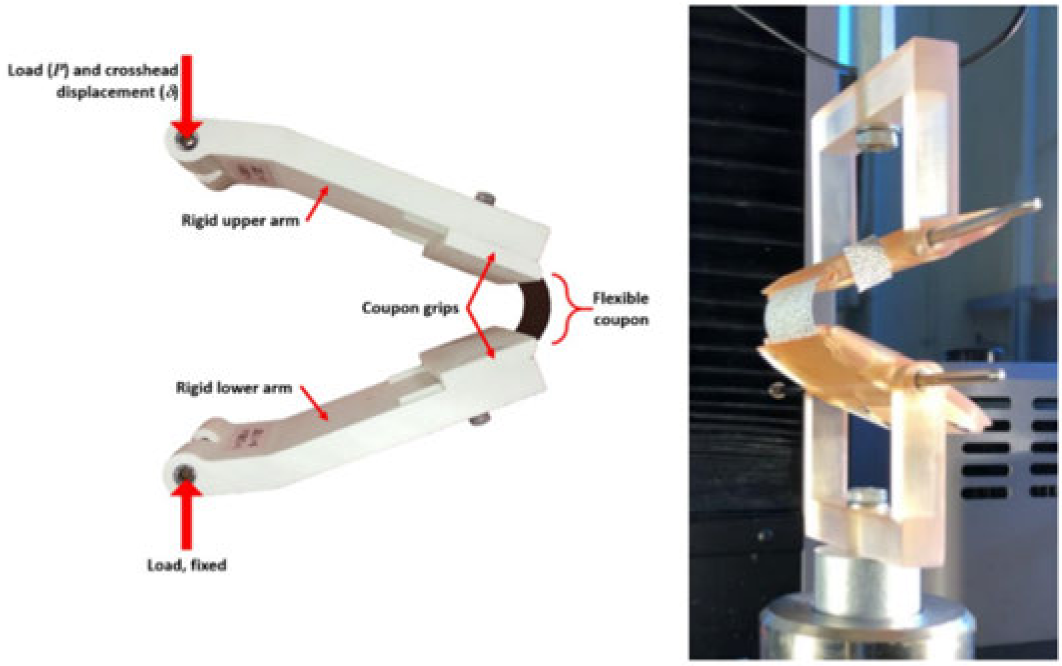

(a) (b)

Fig. 2.7 (a)Weight Un-Balanced Column Bending Test (b) Counter Weight Balanced-Column Bending Test (CWB-CBT)

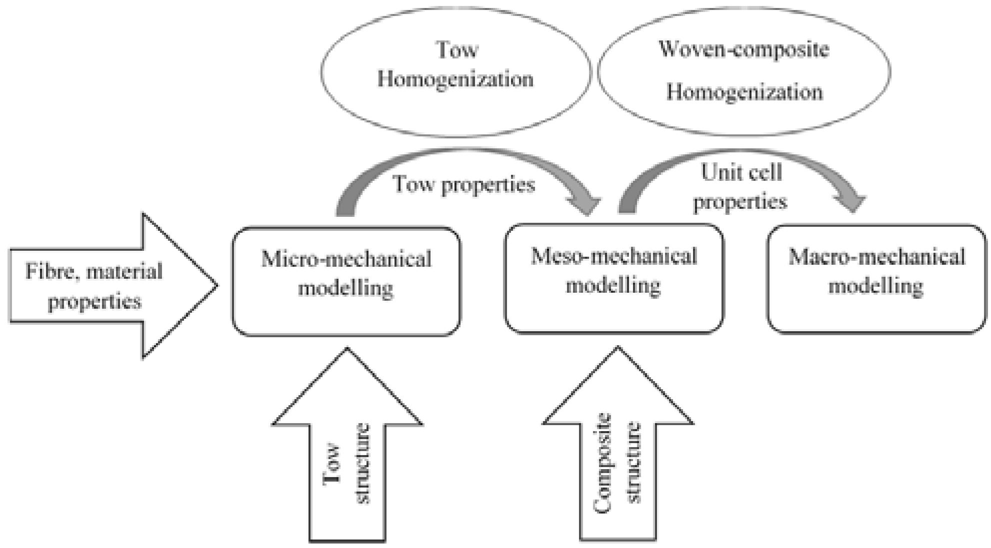

Fig. 2.8 Multi-scale modelling approach

defined by fibre diameter, layer thickness, and laminate thickness, arranged hierarchically as shown in Figure 2.8.

The multi-scale modelling technique is particularly well-suited for composite structures, especially those made from fibre-reinforced composites, as evidenced by prior studies [11, 40, 39]. For deployable composite booms, an iterative multi-scale approach can be employed to achieve high accuracy in capturing their mechanical response. At the macro-scale, which considers the entire boom structure, bending stiffness is continuously updated by integrating results from micro-scale simulations that capture the intricate behaviour of the woven composite material.

This coupling between scales is essential for accurately describing the boom's response, as it allows for the progressive refinement of the material's constituent properties in line with the displacement and rotation patterns observed in the deformed boom, as depicted in Figure 2.9. Developing a robust and reliable model to predict variations in bending stiffness is a critical initial step in this multi-scale modelling process. Recent advancements, such as non-linear computational homogenization and concurrent modelling frameworks, have further enhanced the capability to bridge scales effectively, making multi-scale approaches indispensable for optimizing the design and performance of deployable composite structures for aerospace applications.

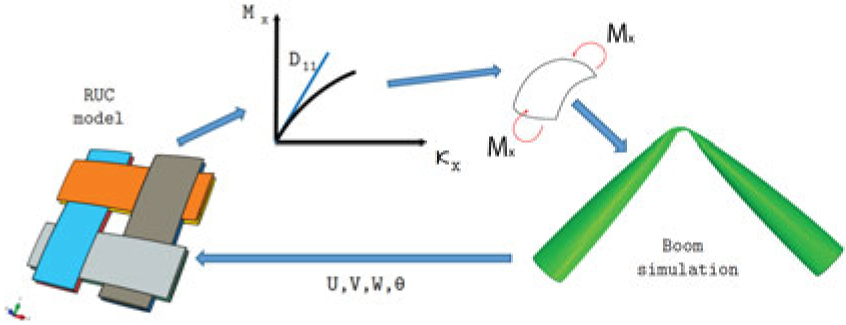

Fig. 2.9 Information transition between the scales to simulate deployable booms

2.6 Analytical methods - Classical lamination theory

The mechanical behaviour of laminates can be effectively predicted using CLT, which has demonstrated excellent accuracy for laminates with unidirectional fibre arrangements. CLT is built upon a set of underlying assumptions, and its suitability for woven fibre composites is examined in detail in this section.

The theory is based on the Kirchhoff-Love hypothesis for shells. The procedure for analysing a specific laminate is as follows:

1. Each individual lamina is analysed, and its behaviour is expressed by relating the in-plane stresses to the in-plane strains and the out-of-plane curvature.

2. The resultant forces and moments acting on the laminate are calculated by integrating the corresponding forces and moments across the thickness of all the laminae. This process leads to the formulation of the **ABD** matrix.

The **ABD** matrix is a standard 6×6 constitutive matrix used to describe the behaviour of any laminate material. It is compactly represented in Equation 2.1 below.

$$\begin{Bmatrix} N \\ -- \\ M \end{Bmatrix} = \begin{bmatrix} A & | & B \\ -- & & -- \\ B & | & D \end{bmatrix} \begin{Bmatrix} \varepsilon \\ -- \\ \kappa \end{Bmatrix} \tag{2.1}$$

Here, **N** represents the in-plane force resultants, **M** represents the out-of-plane moment resultants, and ε and κ denote the in-plane strains and out-of-plane curvatures, respectively [41].

The **ABD** matrix is composed of three sub-matrices: **A**, **B**, and **D**, each containing 9 elements. The **A** matrix defines the relationship between extensional parameters, specifically the in-plane force resultants and strains. The **D** matrix describes the relationship between bending parameters, namely the out-of-plane moment resultants and curvatures. The **B** sub-matrix represents the coupling between bending and extensional parameters.

The expanded form of the **ABD** matrix, which describes the relationships between all in-plane forces, out-of-plane moments, in-plane strains, and out-of-plane curvatures, is provided in Equation 2.2. The x and y directions denote the two principal axes of the laminate.

$$\begin{Bmatrix} N_x \\ N_y \\ N_{xy} \\ -- \\ M_x \\ M_y \\ M_{xy} \end{Bmatrix} = \begin{bmatrix} A_{11} & A_{12} & A_{16} & | & B_{11} & B_{12} & B_{16} \\ A_{21} & A_{22} & A_{26} & | & B_{21} & B_{22} & B_{26} \\ A_{61} & A_{62} & A_{66} & | & B_{61} & B_{62} & B_{66} \\ -- & -- & -- & -- & -- & -- & -- \\ B_{11} & B_{12} & B_{16} & | & D_{11} & D_{12} & D_{16} \\ B_{21} & B_{22} & B_{26} & | & D_{21} & D_{22} & D_{26} \\ B_{61} & B_{62} & B_{66} & | & D_{61} & D_{62} & D_{66} \end{bmatrix} \begin{Bmatrix} \varepsilon_x \\ \varepsilon_y \\ \gamma_{xy} \\ -- \\ \kappa_x \\ \kappa_y \\ \kappa_{xy} \end{Bmatrix} \tag{2.2}$$

The primary assumption of CLT is that the middle sections of the laminate remain straight and perpendicular to the mid-surface during extension or bending. This implies that the shear stresses perpendicular to the mid-surface are zero, i.e., $\gamma_{xz} = \gamma_{yz} = 0$. Additionally, CLT assumes that the bonds between layers are infinitesimally thin, non-shear deformable and that fibres and the matrix are uniformly distributed with a constant thickness for each lamina.

However, in the case of woven fibre composites, many of these assumptions are invalid. This is primarily due to tow waviness, variations in thickness arising from the geometry, and uneven fibre distribution. Since the laminate constitutive relationship in CLT is derived through integration across the thickness, the mechanical behaviour is highly dependent on the thickness. For woven laminates with three or more plies, CLT provides results that closely match experimental observations. However, for single- or two-ply laminates, CLT has been shown to overpredict the bending stiffness by approximately 300% and the maximum bending stiffness by about 400% [10].

This significant discrepancy highlights the influence of the relative positioning of laminae on the mechanical behaviour of one- or two-ply laminates. In aerospace applications, two- to three-ply laminates are often preferred, as an increased number of plies raises the risk of cracking under high curvatures. To address these challenges, meso-mechanical modelling techniques have proven effective in accurately capturing the behaviour of woven fibre composites. The constitutive relationships obtained from such modelling approaches are typically expressed in the form of the **ABD** matrix, similar to CLT.

Chapter 3

Experimental Investigation

This chapter elaborates on the experimental study conducted on thin woven fibre composites to characterise their flexural behaviour using the column bending test method and its analysis.

The CWB-CBT described in section 2.4 was used in this study and three distinct methods were followed to construct the complete bending response in order to assess the viability of each approach. Geometric closed-form solution, Euler's Elastica solution and Direct DIC readings were used. The purpose of using a geometric closed-form solution is to construct the moment-curvature response without using any pre-known material properties of the tested specimen with a simple geometric approach [33]. Euler's Elastica solution accounts for the large deflections of slender elements. It is utilized here to confirm the results obtained from the geometric solution as it can model the actual behaviour of the tested specimen without geometric assumptions [38]. Both of these analyses do not account for any material non-linearity factors, therefore, they display only the geometric non-linearities associated with the deformation. Finally, an analysis was performed using direct DIC measurements of displacement and curvature captured during the experiment, which exhibits a more accurate response as it does not use any conjecture.

3.1 Description of the experimental setup

The main objective of the flexural test conducted in this study is to capture the entire-moment curvature response of a thin woven fibre composite up to failure. The CBT loads the specimen in compression with pinned ends offset from its neutral axis, generating a stress state closer to pure bending. The slope of the moment-curvature curve obtained from the test yields the bending stiffness, D_{11} of the material as a function of the applied curvature, revealing any potential non-linearities. Figure 3.1 shows the experimental setup used in this study.

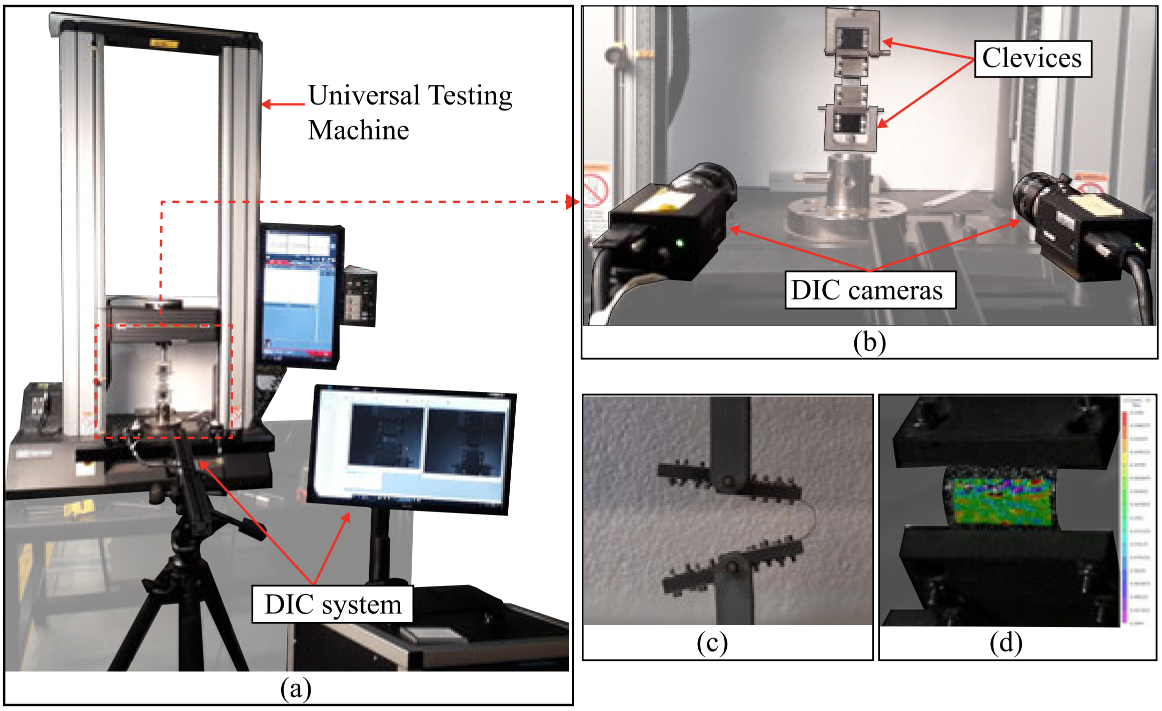

Fig. 3.1 Column bending test: (a) overall experimental setup (b) zoomed view of test space (c) side view of the specimen being bent (d) Digital Image Correlation results plot on top of the deformed specimen.

A two-ply plain woven fibre composite sample made from T300-1k fibres and PMT-F4 epoxy resin was used for the experiment. Two-ply lay-ups of resin-impregnated fabric were cut to the required dimensions and cured in an autoclave under vacuum for 2 hours at 125°C and under a pressure of 600 kPa. The fibre volume fraction, V_f , of the sample was calculated to be 0.62 by weighing five 100 mm $\times$ 100 mm square pieces. The nominal thickness of the laminate was 0.24 mm. The properties of the material are elaborated in table 4.1. A rectangular specimen taken out from the prepared sample with 50 mm $\times$ 20 mm dimensions was vertically aligned and clamped between the two rigid arms. The rigid arms are connected through ball bearings to two rotary shafts to reduce the friction which remains horizontal and parallel during the test. Each shaft is connected to a U-shaped clevice. The bottom clevice is fixed to the Instron 5569 UTM base and the top clevice is fixed to the moving head of the UTM supporting a 10 N loading cell. The moving head was moved downward at a steady rate of 0.17 mm/s to obtain the quasi-static bending response of two-ply laminate [38].

When the moving arm moved downward, the top rotary shaft moved closer to the bottom shaft causing the rigid arms to rotate. Initially, an offset ΔX was introduced between the loading axis and the specimen by securing the specimen to the rigid arms with an eccentricity.

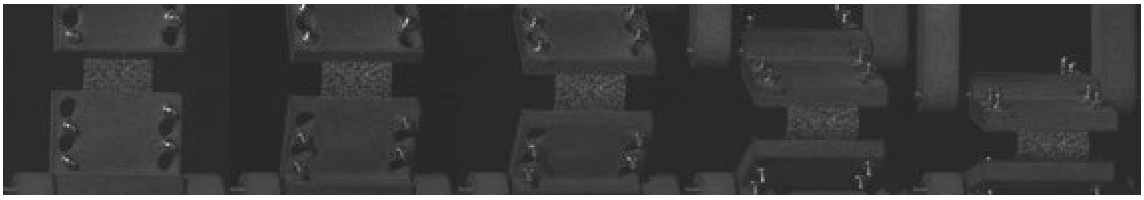

Fig. 3.2 A series of snapshots taken from the left camera during CBT

This created an initial angle, θ between the arms and the loading direction, resulting in the generation of a moment in the specimen and causing it to bend in a predetermined direction when the clevises moved towards each other. The forces generated during the test are very small hence the readings are sensitive to gravity-induced effects. CWB-CBT method described in the section 2.4 was employed in this experiment that uses rigid arms which are symmetric around their connection to the rotary shaft so that they are balanced in the absence of loading. Due to symmetry, lack of gravity effects and the pinned boundary conditions, there is no reaction moment on the grip of the specimen. Therefore, the bending moment in the specimen is equal to the vertical force on the grips times the horizontal distance from the specimen to the pins. This greatly simplifies the calculation of the banding moment.

The applied load and the vertical displacement were recorded from the UTM every 0.02 seconds. A VIC 3D [42] DIC system was used to measure the deformation of the specimen. Matte black coating was applied to the specimen, followed by white speckling, to prepare the surface of the specimen for generating a contrasting random speckle pattern that was required for DIC measurements. Figure 3.2 shows a series of snapshots taken from the left camera during a test. The same procedure was repeated for seven specimens and their geometric details are presented in Table 3.1. All of these specimens failed in the central region by fibre fracture breaking into two separate parts by the end of each test.

Figure 3.3 shows a schematic diagram of the experimental setup indicating the parameters, arm length, l, free length of the specimen, l_s, initial angle, θ, applied load, P and clevis displacement, δ, moment arm length, r and arm rotation angle change, ϕ which are used to calculate the applied moment and curvature using kinematic equations.

The following sections elaborate on the three approaches taken in generating the moment-curvature response using simple geometric analysis, Euler's elastica, and direct DIC measurements.

Table 3.1 Details of two-ply T300-1k/PMT4 coupons used for bending test.

Specimen	Width, w_s (mm)	Free length, l_s(mm)
PW-SP1	20.33	10
PW-SP2	20.00	10
PW-SP3	20.28	11
PW-SP4	20.48	11
PW-SP5	18.34	11
PW-SP6	20.56	11
PW-SP7	21.08	11

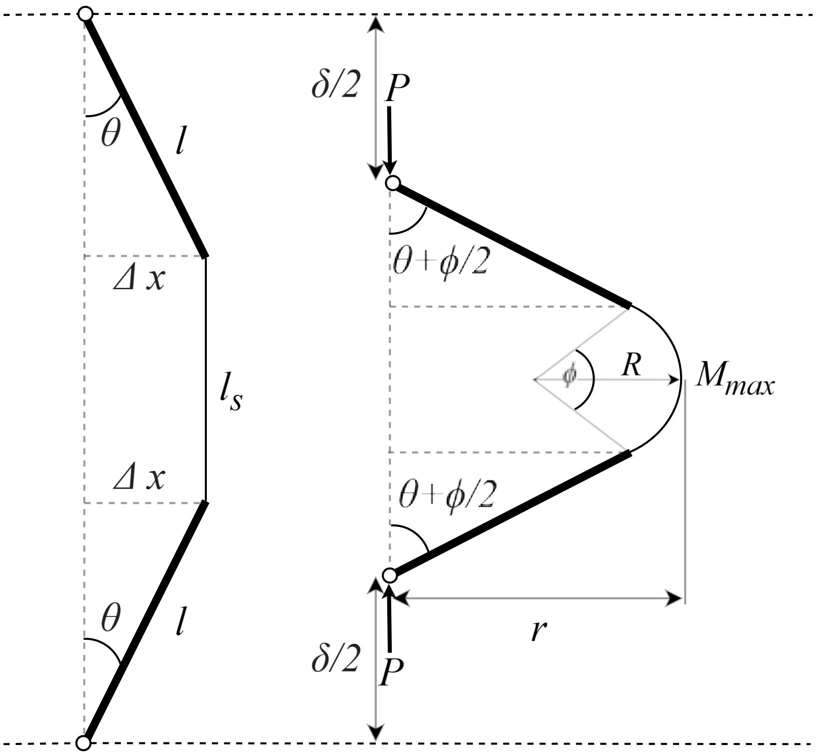

Fig. 3.3 Schematic of the CBT setup

3.1.1 Simple geometric analysis

Using simple geometry P and δ measured from the CBT were processed using the following kinematic relations to obtain the moment-curvature relationship. Assuming a constant curvature along the free length, the curvature of the specimen, κ can be calculated as

$$\kappa = \frac{\phi}{l_s} \tag{3.1}$$

where ϕ is calculated using the following relation.

$$\frac{\delta}{l_s} = 1 - \frac{2}{\phi}\sin\frac{\phi}{2} + 2\frac{l}{l_s}\left(\cos\theta - \cos\left(\theta + \frac{\phi}{2}\right)\right) \tag{3.2}$$

This relationship for ϕ is transcendental and can be solved using MATLAB numerical solver functions.

The maximum moment, M_{max} occurs in the middle of the specimen and can be calculated as,

$$M_{max} = Pr \tag{3.3}$$

where r can be determined using Equation 3.4.

$$\frac{r}{l_s} = \frac{1}{\phi}\left(1 - \cos\frac{\phi}{2}\right) + \frac{l}{s}\left(\theta + \frac{\phi}{2}\right) \tag{3.4}$$

A polynomial interpolation method was utilised using the MATLAB curve fitting toolbox to obtain a smooth and continuous data set to construct the final mean moment-curvature response. Figure 5.1 shows the mean moment-curvature response and standard deviation.

The simplified geometric method assumes a constant curvature along the arc length. This assumption streamlines the problem, deriving the moment-curvature relationship solely from the force and displacement readings obtained from the UTM. Despite its straightforward approach, the assumption of constant curvature (i.e., a circular geometry) may not hold in reality. The curvature varies across the arc length due to the transverse load carried by the specimen, resulting in a maximum curvature at the centre and a minimum at the clamps. Therefore, the validity of this geometric solution should be evaluated.

3.1.2 Euler's Elastica approach

The behaviour of the coupon was modelled using Euler's Elastica, which accounts for the large deflection of slender structural elements. We follow the analysis method presented by

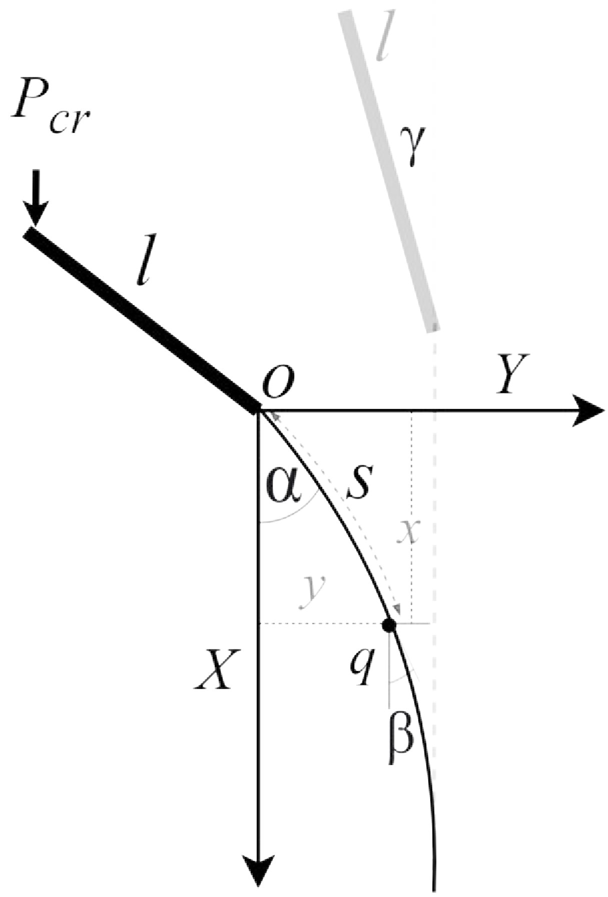

Fig. 3.4 Coupon geometry under large deflections

Gao et al. [38] to compute the Elastica solutions in this study. For clarity, a brief explanation of the method is presented here.

A linear material model is applied in this analysis, and the length of the coupon throughout the experiment is considered constant. The analysis follows the coordinate system depicted in Figure 3.4. Here, o is the origin and X and Y are the vertical and horizontal axes, respectively. q is an arbitrary point on the specimen. The distance from the origin to q along the arc of the coupon is represented as s. β represents the angle between the vector tangent to the coupon and the vertical axis X at q. α is the end slope at the fixture arm. The curvature at q can be expressed as $d\beta/ds$. Therefore, the exact differential equation for the coupon under large deflection is given by,

$$-EI\,\frac{d\beta}{ds} = P_{cr}y + P_{cr}l\sin(\gamma+\alpha) \tag{3.5}$$

where P_{cr} is the critical load. Differentiating Equation 3.5 with respect to s and substituting *dy/ds* $\sin(\beta)$ provide,

$$-EI\,\frac{d^2\beta}{ds^2} = P_{cr}\sin(\beta) \tag{3.6}$$

Multiplying by $d\beta$ and integrating yields,

$$\frac{1}{2}\left(\frac{d\beta}{ds}\right)^2 = k^2\cos(\beta) + \mathrm{C} \tag{3.7}$$

Here, $k^2 = P_{cr}/EI$, and C is an integration constant, which can be determined by applying the boundary conditions at the coupon's top end, where $\beta = \alpha$, with a bending moment of $P_{cr}\cdot l\cdot\sin(\gamma+\alpha)$.

$$\begin{cases} -\frac{d\beta}{ds} = \frac{M}{EI} = \frac{P_{cr}\cdot l\cdot\sin(\gamma+\alpha)}{EI} \\ \mathrm{C} = \frac{1}{2}\left(P_{cr}\cdot l\cdot\sin(\gamma+\alpha)\cdot\frac{1}{EI}\right)^2 - k^2\cos(\alpha) \end{cases} \tag{3.8}$$

Substituting Equation 3.8 in Equation 3.7 gives,

$$\left(\frac{d\beta}{ds}\right)^2 = 2k^2(\cos\beta - \cos\alpha) + \left(\frac{P_{cr}\cdot l\cdot\sin(\gamma+\alpha)}{EI}\right)^2 \tag{3.9}$$

Hence, the solution for ds constructed as

$$ds = -\frac{d\beta}{A}; A = \sqrt{2k^2(\cos\beta - \cos\alpha) + \left(\frac{P_{cr}\cdot l\cdot\sin(\gamma+\alpha)}{EI}\right)^2} \tag{3.10}$$

Total free length of the coupon is obtained by integrating the Equation 3.10.

$$S = 2\int_0^{\alpha}\frac{d\beta}{A} \tag{3.11}$$

The coupon shape can be calculated by solving the differential equations for the position coordinates $x(s)$ and $y(s)$ given in terms of the angle $\beta(s)$.

$$\frac{dx}{ds} = \sin(\beta) \tag{3.12}$$

$$\frac{dy}{ds} = \cos(\beta) \tag{3.13}$$

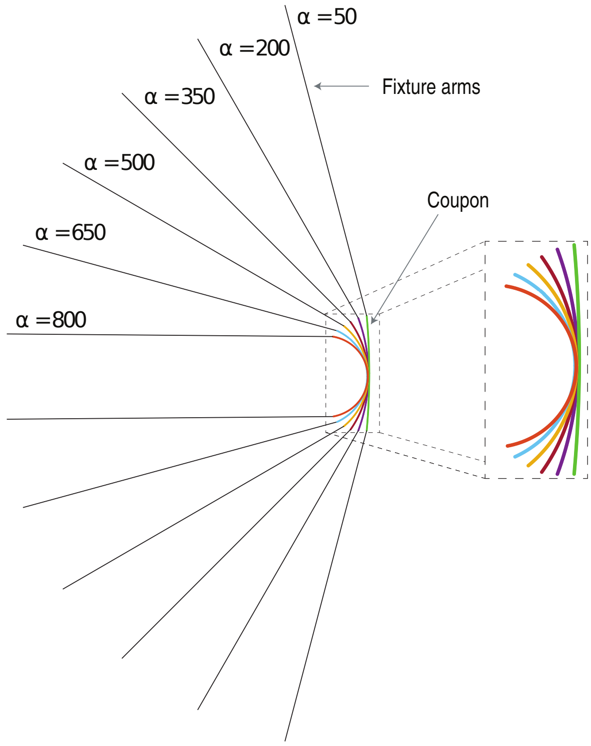

Fig. 3.5 Elastica coupon shape with varying fixture arm end slope.

At any location on the curve where $\beta = \beta'$, the coordinates are calculated by integrating 3.12 and 3.13,

$$x_{\beta'} = \int_{\beta'}^{\alpha} \frac{\cos(\beta)}{A} d\beta \tag{3.14}$$

$$y_{\beta'} = \int_{\beta'}^{\alpha} \frac{\sin(\beta)}{A} d\beta \tag{3.15}$$

The equations delineated above were numerically integrated utilizing MATLAB. The solution provides P_{cr} and coupon shape with defined α, γ, EI and L. The shapes of the coupon, derived using the Elastica solution for varying α are shown in Figure 3.5.

It should be noted that in this CBT experiment, the specimen's geometry under loaded conditions strongly depends on the bending response of the material. The Elastica theory follows a linear material model with a constant bending rigidity EI. However, composites with non-linear constitutive models suggest that the bending rigidity varies with local strain values [43]. This consideration further amplifies the error in the simplified geometrical solution, making the Elastica theory solution an upper-bound solution for composites with non-linear constitutive behaviours. Therefore, it is necessary to evaluate the bending behaviour of the composite using a direct experimental measurement technique such as DIC to comprehend the real bending behaviour of the material accurately.

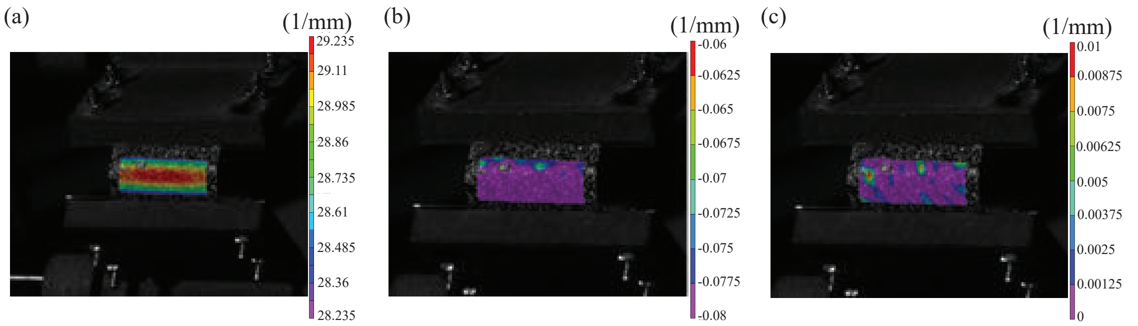

Fig. 3.6 Full-field deformation results obtained through DIC measurements for PW-SP1 specimen: (a) Out-of-plane deformation (b) Longitudinal curvature (c) Transverse curvature.

3.1.3 Direct measurements with DIC

The DIC system provides direct measurements of displacement and curvature values, which can be used to construct the moment-curvature response without any conjecture. A VIC 3D DIC system was used capture the deformation in this experiment. Figure 3.6 shows out-of-plane displacement, longitudinal curvature and transverse curvature variation plots on top of the deformed specimen. The maximum out-of-plane deflection occurs at the central region and spreads uniformly across the width of the specimen as shown in figure 3.6(a). The distribution of longitudinal curvature is fairly uniform across the specimen as expected in a pure bending scenario as demonstrated in Figure 3.6(b). The transverse curvature is negligible as shown in Figure 3.6(c) except for the regions near the boundary of the region of interest. Due to the large out-of-plane deformation of the test it is not possible to capture precise deformation measurements for the entire region of interest. The irregularities seen in the top part of the contour plots resulted due to the reflection of light on the right camera of the DIC system at large curvatures. The DIC system was arranged to capture the deformation of the central region of the specimen throughout the test. Therefore, deformation quantities were extracted for a 2 mm tall window spanning across the width of the central region of the specimen for moment-curvature investigations performed in this study.

Force readings from the UTM were multiplied by the corresponding lever arm obtained from DIC measurements to calculate the applied moment for each curvature measurement. A third-degree polynomial curve fitting method was applied to each trial to generate a smooth and continuous moment-curvature response. The complete non-linear region of the accurate bending response can be observed by this technique compared to the analytical interpretations described in Sections 3.1.1 and 3.1.2. Furthermore, extrapolated initial bending stiffness indicates a clear reduction of bending stiffness at high curvatures.

Chapter 4

Multi-scale Modelling

This study extends beyond the experimental analysis of the thin woven fibre composites under large curvature by proposing a novel methodology to simulate the accurate non-linear kinematic behaviour of structures made from thin woven fibre composites. The proposed method is broadly applicable to other thin-shell structural materials with strain-dependent sectional properties.

This section introduces the proposed multi-scale modelling approach to capture the non-linear bending behaviour observed in the experimental study. The approach begins with micro-scale homogenization of the tows to determine their effective properties. Using these homogenized tow properties, along with a previously developed meso-scale RUC by Weerasinghe and Mallikarachchi (2022) [16], the meso-scale response of the laminate is obtained. Finally, the meso-scale bending response of the material is integrated into a macroscale model to simulate a structural component subjected to pure bending, enabling the observation of the laminate's non-linear kinematic behaviour. This comprehensive process forms the basis for concluding the study.

4.1 Micro-scale analysis

4.1.1 Homogenisation of tow Properties - linear region

The laminate considered in this study is a two-ply plain woven composite laminate made of T300-1K carbon fibres and PMT-F4 resin. Properties of the constituents obtained from the manufacturer are presented in table 4.1. Tows are idealized as a three-dimensional continuum with transversely isotropic material properties. To represent a transversely isotropic continuum, five independent engineering constants are required. Those constants of the tows in the materially linear region were calculated using the Halpin-Tsai semi-empirical relation and Rule of Mixtures. As mentioned in chapter 3, the fibre volume fraction considered in these calculations is 0.62.

Table 4.1 Material properties of T300-1k fibres and PMT-F4 epoxy resin

Constituent Property	T300 Fibres [44]	PMT-F4 Resin [45]
Longitudinal stiffness, E_1 (N/mm^2)	233,000	3,833
Transverse stiffness, E_2 (N/mm^2)	23,100	3,833
Shear stiffness, G_{12} (N/mm^2)	8,963	1,441
Poisson's ratio, ν_{12}	0.20	0.33
Density, ρ (kg/m^3)	1,760	1,210
Areal weight of fabric, W (g/m^2)	98	-

Effective longitudinal stiffness and Poisson's ratio were obtained using the rule of mixtures:

$$E_1 = E_f V_f + E_m(1 - V_f) \tag{4.1}$$

$$\nu_{12} = \nu_{13} = \nu_{12f} V_f + \nu_m(1 - V_f) \tag{4.2}$$

Transverse stiffness and shear modulus were determined using the Halpin-Tsai equations:

$$E_2 = E_3 = E_m \frac{1 + \chi \eta V_f}{1 - \eta V_f} \tag{4.3}$$

where

$$\eta = \frac{E_{2f} - E_m}{E_{2f} + \chi E_m} \tag{4.4}$$

Here, the parameter χ is a measure of the reinforcement of the composite, taken as 2 [46].

$$G_{12} = G_{13} = G_m \frac{(G_{12f} + G_m) + V_f(G_{12f} - G_m)}{(G_{12f} + G_m) - V_f(G_{12f} - G_m)} \tag{4.5}$$

Finally, the in-plane shear modulus G_{23} is taken as stated in Quek et al. [47], and the transverse Poisson's ratio was calculated as:

$$G_{23} = \frac{E_2}{2(1 + \nu_{23})} \tag{4.6}$$

With the above techniques, the calculated effective material properties of the tow is presented in Table 3.3.

Table 4.2 Estimated mechanical properties of cured T300-1k/PMT-F4 tow.

Tow property	Value
Longitudinal stiffness, E_1 (N/mm^2)	145,920
Transverse stiffness, $E_2 = E_3$ (N/mm^2)	11,132
Shear stiffness, $G_{12} = G_{13}$ (N/mm^2)	3,782
In-plane shear stiffness, G_{23} (N/mm^2)	3,680
Poisson's ratio, $\nu_{12} = \nu_{13}$	0.249
Poisson's ratio, ν_{23}	0.512

Note that these tow properties belong to the linear region of the deformation. According to the material non-linearity of the fibres described in section 4.1.2, tows have a strain dependant material behaviour which will be described in the same section.

4.1.2 Stiffness non-linearity in carbon fibres

Carbon fibre's nano-structure consists of sheets of carbon atoms which are not fully aligned with the fibre direction. These sheets of carbon atoms rotate and align with the fibre direction when a longitudinal positive strain (Tensile strain) is applied to a fibre increasing the fibre's directional stiffness and softening the fibres under negative longitudinal strain (Compressive strain). This phenomenon is interpreted as the inherited stiffness non-linearity of the carbon fibres [48]. The same behaviour can be observed in carbon fibre laminates loaded under tension or bending [49, 50]. Several constitutive relationships have been proposed to determine and model this nonlinear behaviour. The model we use in this study is an empirical relation proposed by Van Dreumel and Kamp [51]. It proposes a quadratic dependence on the stress-strain relationship which yields an accurate approximation for most carbon fibres. The modulus of the fibers, E_f, is given by

$$E_f(\varepsilon) = E_0(1 + \gamma\varepsilon) \tag{4.7}$$

where E_0 is the initial stiffness of the fiber, ε is the applied strain, and γ is a parameter that determines the level of nonlinearity. In our case, for tensile stiffening, we have that $\gamma > 0$. The value of the γ can be different or the same in compression and tension depending on the type of the fibre.

Using this fibre model Murphey et.al [43]. developed a non-linear fiber-based constitutive model to describe the behaviour of thin flexures subjected to large strains. According to this model, only the fibre component is assumed to be non-linear, whereas the matrix behaviour is assumed to be linearly elastic for all strains.

$$E_1 = E_f V_f + E_m(1 - V_f) \tag{4.8}$$

Thus, we obtain different composite moduli for tension E_{1T} and compression E_{1C}, given by:

$$E_{1T} = E_0(1 + \gamma_T \varepsilon)V_f + E_m(1 - V_f) \quad \text{for} \quad \varepsilon \geq 0$$

$$E_{1C} = E_0(1 + \gamma_C \varepsilon)V_f + E_m(1 - V_f) \quad \text{for} \quad \varepsilon < 0$$

Here, E_m represents the matrix modulus and V_f represents the fibre volume fraction of the composite. Here we make the assumption that the axial modulus E_1 of the tows is significantly larger than the transverse modulus E_2. This allows us to neglect the contribution of non-linear E_2 in our moment-curvature relationship making the problem dependent on one major variable material constant. According to this constitutive law, there exists a critical compressive strain ε_{cr} where the instantaneous modulus becomes zero. Beyond this value, non-physical tensile stresses persist with compressive strains. Therefore, imposing three conditions for the bi-modal fibre constitutive law, a unified model can be presented below,

$$E(\varepsilon) = V_f \left(\begin{array}{c} \mathrm{E}_b \ [\varepsilon < \varepsilon_{cr}] + E_0(1 + \gamma_C \varepsilon) \ [\varepsilon_{cr} < \varepsilon < 0] \\ + \mathrm{E}_0(1 + \gamma_T \varepsilon) \ [0 < \varepsilon] \end{array} \right) + E_m(1 - V_f) \tag{4.9}$$

where, E_0 is the modulus at zero strain, ε notation is used to indicate a step function that is '1' if the enclosed condition is true and '0' if the condition is false. Here, E_b modifies modulus to be positive near zero at a critical value of compressive strain, ε_{cr}. In this study, the observed maximum compressive strains are less than the critical value, hence the near-zero axial stiffness did not occur. γ_C and γ_T coefficients for T300 fibres were obtained from Keryvin et al. [52], which are 8 and 13 respectively. The implementation of this on-linear material model into the tows in ABAQUS standard will be described in section 4.3.2.

4.1.3 Micro-scale Geometric Properties

X-ray Computed Tomography (XRCT) is a powerful non-invasive imaging technique used to examine the internal structures of objects enclosed within dense materials. This method was utilized to capture detailed geometric features of the two-ply laminate. The scanning process employed a hard X-ray microtomography beam-line (Beamline 8.3.2) at the Advanced Light Source in Lawrence Berkeley National Laboratory, a state-of-the-art synchrotron light source facility. Samples measuring 8 mm × 3 mm were scanned with high precision using an energy level of 22 keV and achieving a pixel resolution of 1.5 μm.

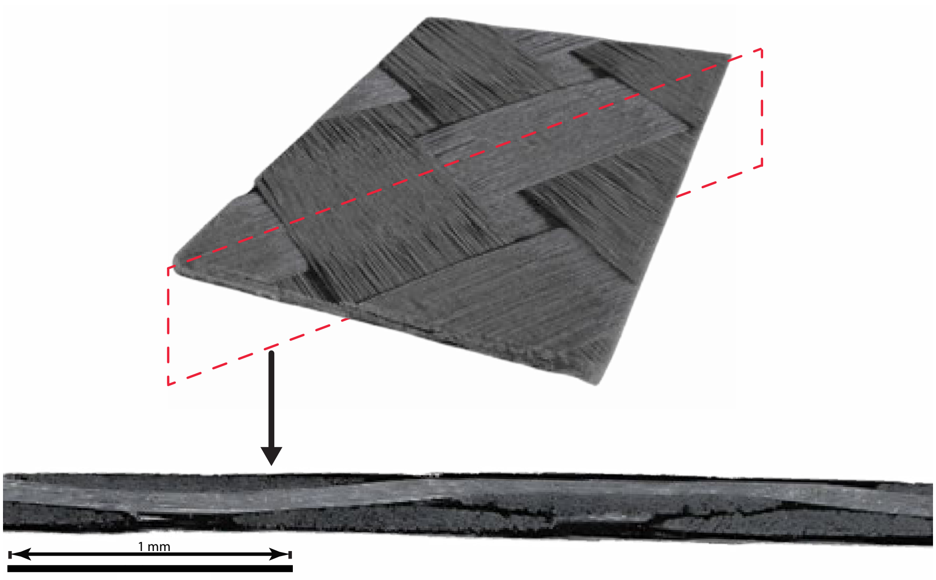

Fig. 4.1 Micro-structure of two-ply plain weave T300/PMT-F4 laminate reconstructed by processing XRCT images.

To reconstruct the captured images, the Super Voxel Model-Based Iterative Reconstruction (SVMBIR) algorithm was implemented. This advanced reconstruction method was selected for its ability to produce smoother and more accurate reconstructions compared to traditional analytical techniques such as Gridrec and Fourier Back Projection. The superior performance of iterative methods ensures finer detailing and improved visualization of the laminate's internal morphology.

Figure 4.1 presents an isometric view and a cross-sectional profile of the laminate derived from the XRCT scans. Scanned image slices are down-sampled and merged in lateral direction using ImageJ software and Dragonfly software was used for the 3D rendering and image segmentation.

Results revealed that the nominal weave length of the plain weave laminate, $\Delta l = 2.88\,\mathrm{mm}$, average tow thickness, $t_{\mathrm{tow}} = 0.06\,\mathrm{mm}$, average tow width, $w_{\mathrm{tow}} = 1.14\,\mathrm{mm}$, and average cross-sectional area of a tow, $A_{\mathrm{tow}} = 0.0518\,\mathrm{mm}^2$. Figure 4.2 shows the procedure of obtaining the measurements from the 3D volumetric images.

4.2 Meso-scale modelling

The woven composite's RUC model was designed to accurately capture the realistic microstructural arrangement of tows. This detailed geometry was then used to simulate the mechanical response under conditions of high curvature, focusing exclusively on non-linear

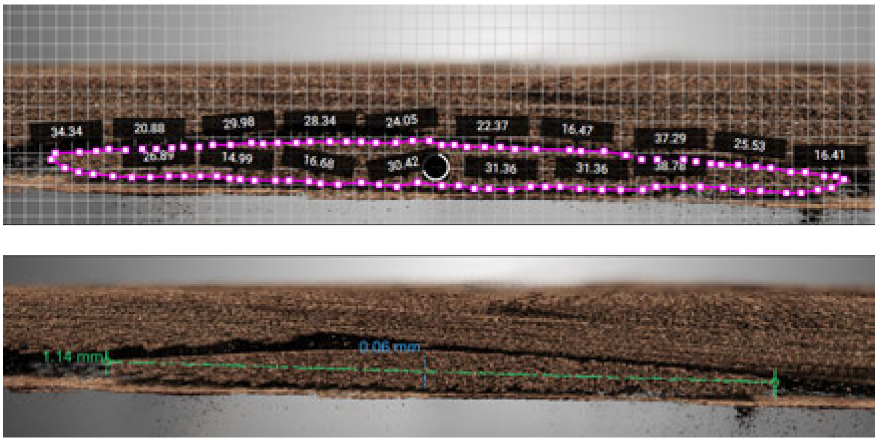

Fig. 4.2 Micro scale geometric measurements from the XRCT reconstruction

geometrical effects while assuming linear material behaviour. This approach aimed to isolate the impact of complex geometric deformations on bending performance.

To further refine the analysis, the influence of inter-tow interactions was incorporated by introducing cohesive interactions between the tows. Building on this, an advanced analysis was conducted, integrating both geometrical and material non-linearities. This allowed for a comprehensive investigation into the constitutive behaviour of the tows and its influence on the macroscopic response, providing a more realistic representation of the composite's bending behaviour.

4.2.1 Geometric modelling of RUC

The geometry of the two-ply plain woven RUC presented in this work, is characterised by confirming the geometrical properties (i.e. Weave length, tow cross-section, ply arrangement, etc.) obtained by the 3D XRCT analysis described in section 4.1.3. Following the sensitivity analysis performed by Gowrikanthan et al. [53], a 2 $\times$ 2 RUC was created to have the optimum computational cost while achieving the desired level of accuracy. Even though, there could be misalignments and phase differences between the two plies in real cases, only fibre-in-phase arrangement was considered for the numerical model adhering to findings from phase sensitivity analysis done by Gowrikanthan et al. [53]. A cubic Bezier curve, which follows the tow architecture observed in XRCT images, has been fitted along the length of the tows to generate the tow profile. Equation 1 characterises the cubic B ´ezier spline used to represent the towpath.

$$B(k) = P_0(1-k)^3 + 3P_1(1-k)^2 + 3P_2k^2(1-k) + P_3k^3, \quad 0 \leq k \leq 1 \tag{4.10}$$

where k is a non-dimensional parameter representing a location on the line, and points P_0, P_1, P_2, and P_3 are defined based on the properties of the tow geometry considered.

Parametric coordinates of the idealised tow cross-section are given by $\mathbf{C}(t) = (C_x(t), C_y(t))$, where $t \in [0.0, 1.0]$. $C_x(t)$ and $C_y(t)$ are given by

$$C_x(t) = \frac{w}{2}\cos(2\pi t), \quad 0.0 \leq t \leq 1.0 \tag{4.11}$$

$$C_y(t) = \begin{cases} \frac{h}{2}\sin(2\pi t)^n, & \text{if } 0.0 \leq t \leq 0.5 \\ -\frac{h}{2}\left(-\sin(2\pi t)\right)^n, & \text{if } 0.5 < t \leq 1.0 \end{cases} \tag{4.12}$$

where h, w, and n are the minor diameter, major diameter, and power of the cross-section, respectively. For the woven composite considered in this paper, $n = 0.5$ is found to be the best-fit value to model the observed cross-section. The idealised tow cross-sectional area is given by

$$A_{\text{tow}} = 0.278\pi hw \tag{4.13}$$

Each tow was discretised using the same TexGen FE pre-processor, utilising eight-node linear reduced integration brick elements (`C3D8R`) and six-node linear triangular prism elements (`C3D6`). This selection aims to minimise any artificial increase in geometric stiffness and allows for non-prismatic shapes. Furthermore, the number of through-thickness mesh layers was increased to four using a built-in Python console to avoid zero energy modes during the analysis.

To simulate the realistic contact geometry while avoiding mesh distortions and skewed elements due to overlapping at contact regions, built-in *Adjust Intersections* tool has been employed considering 0.005 mm overlapping tolerance value.

Subsequently, the input file ($*$.*inp*) is imported to Abaqus/Standard finite element software package [54] in the form of an orphan mesh to perform mechanical simulations, Figure 4.3. The appropriate element size was selected following Gowrikanthan et al. [53].

4.2.2 Periodic boundary conditions

Periodic boundary conditions have been employed in this homogenisation procedure over displacement or traction boundary conditions to enrich the representativeness and size effect towards the continuum nature. The general form of the utilised boundary conditions is given by,

$$x_M^+ - x_M^- = F_M.(X_M^+ - X_M^-) \tag{4.14}$$

Fig. 4.3 Representative Unit Cell of two-ply plain weave laminate used for numerical modelling. Each colour represents a separate tow.

where, F_M is the macro-scale deformation gradient tensor, X_M and x_M are the position vectors in reference and deformed configurations, respectively. Meso-scale micro-fluctuations, w_m and the normal vectors, n_m at the boundary have been considered to be anti-periodic to fulfil the requirements stated in Equation 4.14. Hence,

$$w_m^+ = w_m^- \tag{4.15}$$

$$n_m^+ = n_m^- \tag{4.16}$$

Adhering to these general forms, the procedure suggested by Mallikarachchi [55] was enforced in the meso-scale model using equation constraints applied on the reference nodes and dummy nodes.

The reference nodes were defined for each pair of boundary nodes of adjacent tows that share the same phase in different plies. A dummy node was introduced to establish the connection between reference nodes by applying equation constraints for every matched pair of these reference nodes located on opposite sides of the RUC. It should be noted that all the reference nodes and dummy nodes are positioned in the neutral plane of RUC to prevent it from inducing any additional moments due to eccentricities, Figure 4.4.

Nodes at the boundaries of both tows are linked to their corresponding reference nodes with MPC beam connectors which enables the coupling of both translational and rotational degrees of freedom. Subsequently, a single dummy node has been established per each pair of opposite reference nodes and linked them, enforcing **Equation* constraints. This allows strains to be directly applied on the dummy nodes throughout the simulation and eliminates imposing local changes in cross-section areas or rigid plate behaviour at the boundaries.

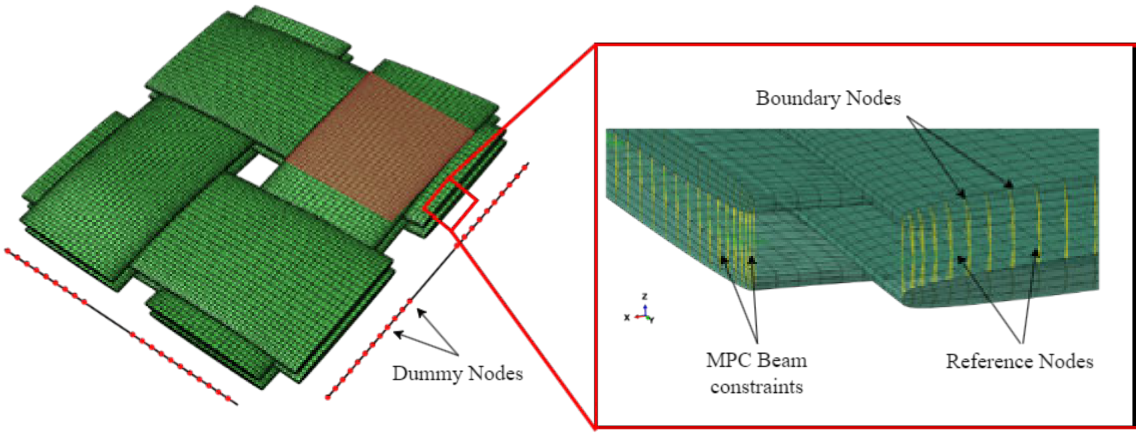

Fig. 4.4 Implementation of periodic boundary conditions in the RUC model

4.2.3 Interaction between tows

The large curvatures experienced by ultra-thin woven composites could result in micro-slipping at the contact regions between tows in both the same ply and different plies. Simulating the realistic slipping behaviour is vital in this analysis due to the conjecture that micro-slipping is a key feature driving the observed bending stiffness reduction in higher curvatures. Abaqus/Standard provides surface-based cohesive contact behaviour and element-based cohesive contact behaviour for simulating slip between two contact surfaces. Element-based cohesive behaviour is more effective in simulating conditions where localised contact phenomena are dominant. In this case, utilising element-based contact behaviour can lead to mesh distortions and deceptive results due to the complexity of the geometric architecture and extremely thin interaction zones. As the alignment of surface mesh is near-perfect, surface-based contact behaviour with cohesive constraints characterised by linear elastic traction-separation behaviour is competent in simulating the actual effect of resin at contact regions.

Bi-linear traction separation law served as the foundation for defining the interface behaviour of surface-based cohesive contact. The elastic behaviour is characterised by a stiffness matrix relating normal and shear stresses to corresponding normal and shear separations along the interface. The relationship between stresses and separations is defined as,

$$\begin{bmatrix} t_n \\ t_s \\ t_t \end{bmatrix} = \begin{bmatrix} k_{nn} & 0 & 0 \\ 0 & k_{ss} & 0 \\ 0 & 0 & k_{tt} \end{bmatrix} \begin{bmatrix} \delta_n' \\ \delta_s' \\ \delta_t' \end{bmatrix} \tag{4.17}$$

where t and δ' represent stress and separation displacement, respectively. The subscript, n denotes the normal direction, while subscripts s and t represent the two transverse shear directions. The parameter k_{nn} corresponds to the normal stiffness, while k_{ss} and k_{tt} correspond to the shear stiffness in the two perpendicular directions. The following method to find the cohesive constants was proposed by Wijesuriya et al. [56] and is described here for clarity. An uncoupled behaviour of the normal and tangential stiffness components is assumed, which means that pure normal separation does not occur with any cohesive force in the shear direction and vice versa. To simulate the matrix response at contact regions, interaction behaviour was established using finite element analysis focused solely on the matrix. A resin block of 1 mm $\times$ 2 mm $\times$ 0.01 mm with a pre-introduced 0.5 mm crack was modelled in ABAQUS using XFEM, allowing simulation of crack initiation and propagation without re-meshing. Material properties and tensile strength from manufacturer data were applied, and the model was meshed with C3D8R elements. The analysis provided opening displacement and normal stresses to calculate k_{nn}, estimated at 253,722 MPa/mm, with k_{ss} and k_{tt} calculated as 90,561 MPa/mm, given the resin's isotropic nature. This separate analysis was conducted to simulate the matrix behaviour between tows as an interaction property, thereby avoiding the computational expense of modelling actual finite elements.

4.2.4 Formation of constitutive relationship

The material tangents for the macroscopic behaviour are defined in the form of ABD matrix. Employed periodic boundary conditions in the RUC allow us to idealise the continuum composite as a thin shell using Kirchhoff-Love hypothesis to obtain the constitutive relationship. In-plane deformation kinematics are defined using first-order Taylor series,

$$u = u_0 + \varepsilon_x\, x + \frac{1}{2}\varepsilon_{xy}\, y \tag{4.18}$$

and

$$v = v_0 + \varepsilon_y\, y + \frac{1}{2}\varepsilon_{xy}\, x \tag{4.19}$$

where the x and y are the two in-plane principal directions and u and v the corresponding displacements, respectively. ε is the mid-plane strain. It should be noted that the engineering shear strain and twice the surface twist are used to define the shear strain and twisting curvature, respectively.

The out-of-plane deformation, w can be described using second-order Taylor series expansion as,

$$w = w_0 + \left(\frac{\partial w}{\partial x}\right)_0 x + \left(\frac{\partial w}{\partial y}\right)_0 y + \frac{1}{2}\left(\frac{\partial^2 w}{\partial^2 x}\right)_0 x^2 + \frac{1}{2}\left(\frac{\partial^2 w}{\partial^2 y}\right)_0 y^2 + \left(\frac{\partial^2 w}{\partial x \partial y}\right)_0 xy \quad (4.20)$$

Then, the constitutive relationship is defined as described in section 2.6.

It is important to note that while the ABD matrix has been employed as the constitutive relationship for the material, particular emphasis has been placed on the [D] sub-matrix, which describes the bending behaviour in the subsequent sections. This focus is due to the study's objective of analysing the composite's flexural behaviour.

Despite the observed strains in ultra-thin composites being higher compared to the deformations that can be observed in thick woven composites, those can still be considered in the small strain range defined in Abaqus ($< 5\%$). Therefore, constitutive laws used in defining transversely isotropic material are valid for simulations in both linear and non-linear regimes.

Abaqus internally converts the specified engineering constants to the appropriate material model parameters for the specified constitutive model to accommodate large strains. Here, a hyper-elastic constitutive model based on strain energy potential which is compatible with the input parameters used for transversely isotropic material was defined. The general polynomial form of the strain energy function was defined as,

$$U = \sum_{i+j=1}^{N} C_{ij}(I_1 - 3)^i (I_2 - 3)^j + \sum_{i=1}^{N} \frac{1}{D_i}(J_{el} - 1)^{2i} \quad (4.21)$$

where U is the strain energy potential, J_{el} is the elastic volume ratio, I_1 and I_2 are measures of distortion in the material and C_{ij}, D_i are material parameters. Here, the first part of the model describes the elastic deformation response of the material, and the second part imposes a penalty to induce incompressibility of the material.

First, six separate strain analyses were performed on the RUC while employing linear material properties presented in Section 4.1.1 for tows. The corresponding ABD matrices were calculated using the principle of virtual work. Accordingly, each analysis was conducted enforcing predetermined deformation on a single kinematic variable while keeping deformations of all other kinematic variables at zero (i.e, when $\varepsilon_x = 1$, $\varepsilon_y = \varepsilon_{xy} = \kappa_x = \kappa_y = \kappa_{xy} = 0$). Then the rotations and displacements at the boundary nodes, along with the corresponding moments and forces of the dummy nodes, were extracted from each analysis to calculate corresponding entries of the ABD matrix. The first component $ABD_{1,1}$ calculated using virtual work is given by,

$$N_{xx}\varepsilon_{xx}\Delta l_x\Delta l_y = \sum (F_x u + F_y v + F_z w + M_x\theta_x + M_y\theta_y + M_z\theta_z) \tag{4.22}$$

Similarly, all entries were calculated using virtual work calculations performed on all six analyses and were entered into a tensor form to formulate the ABD stiffness matrix. Three displacements and three rotations for each of the 1392 boundary nodes were combined into the displacement matrix, $U(1392 \times 6)$ and corresponding forces and couples of each boundary node have been combined into the force matrix, $F(1392 \times 6)$ for each particular case. Hence the stiffness matrix can be calculated as,

$$ABD = \frac{U^T F}{\Delta l_x . \Delta l_y} \tag{4.23}$$

The six separate analyses required to formulate the ABD stiffness matrix are preformed by setting individual strain or curvature in one direction at a time while restraining the remaining five at zero. This induces a noise due to the Poisson's effect at the boundaries. This effect is smoothed by the incompressibility penalty introduced through Equation 4.21 to the finite element mesh. Since the principle of virtual energy was applied over the entire model in calculating the ABD matrix, the final quantities are independent of this effect.

4.3 Modelling non-linear finite strain behaviour

One of the key contributions of this study is to introduce geometric and material non-linearity into the meso-mechanical homogenisation model on thin woven composites. This section describes incorporating geometric non-linearity and material non-linearity of tows in the numerical model. A user-defined subroutine was developed to update the elastic properties of tows with the degree of deformation.

4.3.1 Non-linear geometric analysis

Formation of non-linear geometric response requires extracting forced and deformation quantities in an incremental manner. Therefore, following the method described in Section 4.2.4, six separate geometrically non-linear analyses were performed employing 0.2 mm^{-1} maximum curvature or 0.2 maximum axial strain values. Subsequently, force and deformation variables for each analysis were extracted in equal time intervals, and the applied curvature after each time period was calculated by linearly interpolating between time intervals. Then, the corresponding constitutive relationship for each curvature value was computed from extracted data following Equation 4.23.

4.3.2 Incorporating non-linear constitutive law

The model described so far assumed a constant elastic modulus for the tows throughout the analysis. However, as the section 4.3 presented, tows demonstrate non-linear elastic response when subjected to large deformations [43]. In order to assess the effect of tow non-linearity, the bi-modal constitutive law described in the section 4.3 was incorporated into the meso-modal.

Abaqus provides different options to model hyper-elastic material of this nature, with built-in material models (Mooney Rivlin, Ogden), experimental data fitting models, material calibration methods, and user-defined material subroutines. *USDFLD* user-defined subroutine was selected to model the material behaviour using Equation 4.9.

The user subroutine updates the material behaviour at the beginning of each iteration. Initially, it generates the stiffness matrix based on the model configuration at the start of the increment. In the next call, it creates a new stiffness matrix reflecting the updated configuration. In subsequent iterations, the subroutine is called once per iteration, with model configurations consistently calculated using the stiffness matrix at the end of the previous iteration.

USDFLD subroutine provides access to solution data after each increment, which allows the definition of material properties as a function of solution data (i.e., $f_i(\sigma, \varepsilon, \varepsilon', etc.)$. This subroutine was used in this study to extract field variable values at current material points that were interpolated from the nodes at the end of the current increment. Updated field variable values are used in calculating values of material properties that are defined as a function of field variables. Figure 4.5 presents the procedure followed in the algorithm.

The axial stiffness of a tow, $E_{11,tow}$ has been fed as a function of axial strain in tabular form for the strain range of [-0.02, 0.02] at a frequency of 0.001. The input strain range was determined by performing a simulation for the same curvature without introducing material non-linearity and obtaining the maximum compressive and tensile stress induced throughout the simulation. Note that Abaqus is using linear interpolation between data points in the tabular input and will be using the last available material data if the field variable value is outside of the specified range without extrapolating.

Since the USDFLD subroutine has access to the material point data only at the start of an increment, the solution dependence introduced in this way inside the increment is explicit, and hence, the material properties for a given increment will not be influenced by the results obtained during the increment. Therefore, the time increment was controlled manually in

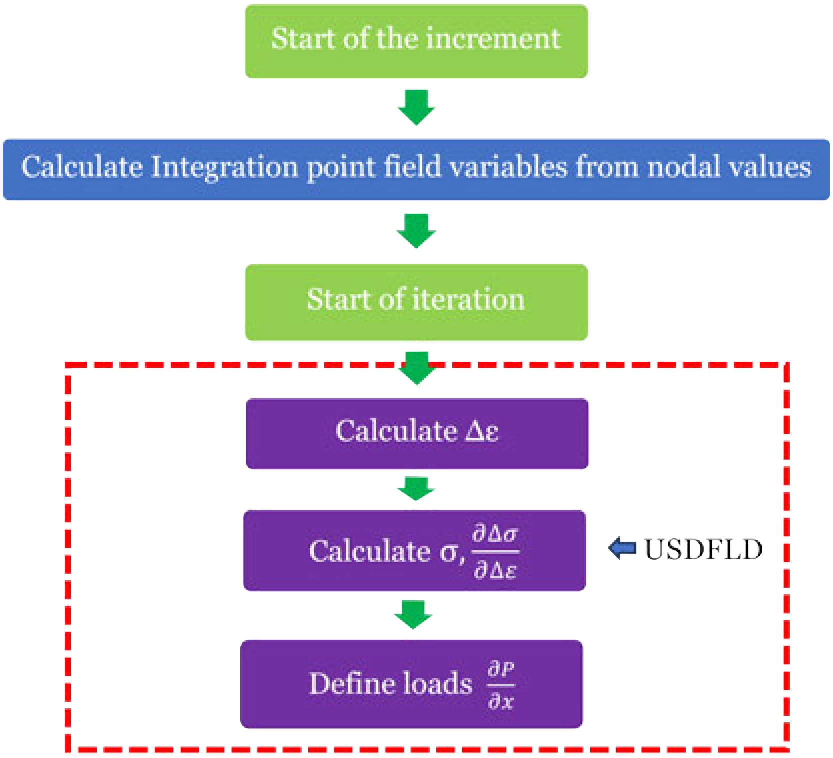

Fig. 4.5 Flowchart of procedure followed in USDFLD subroutine within a time increment.

order to achieve the required accuracy. The automatic time incrementation algorithm defined in Abaqus reduces the size of the time increment when convergence is unlikely, or the results are not accurate enough. Using the PNEWDT function, we set a large enough time increment value before each call to USDFLD; thus, the simulation can use a larger increment size initially and may increase the time increment if the solution converges in the current iteration.

Furthermore, in the case of non-linear material analysis, the material constituents are specified as a function of solution-dependent variables such as strain. USDFLD subroutine allows to define material parameters as a function of the material point data and material directions. This access is made independently at each "constitutive calculation point," which, in this case, is the numerical integration point in each element. Thus, the constitutive routines are concerned only with a single calculation point. The element provides an estimate of the kinematic solution to the problem at the point under consideration. These kinematic data are passed to the constitutive routines as the deformation gradient or typically the strain and rotation increments.

From a numerical viewpoint, the implementation of a constitutive model involves the integration of the state of the material at an integration point over a time increment during a non-linear analysis. It should be noted that the implementation of constitutive models in Abaqus assumes that the material behaviour is entirely defined by local effects, so each spatial integration point can be treated independently. Since Abaqus/Standard is most commonly used with implicit time integration, the implementation must also provide an accurate “material stiffness matrix” for forming the Jacobian of the non-linear equilibrium equations. As a result, updating the material definition independently at each material point will not affect the accuracy or integrity of the model.

As discussed in Section 4.3.1 same procedure was followed to extract displacements and rotations of each dummy node and corresponding forces and moments of reference nodes at the end of each increment. Subsequently, the corresponding constitutive relationship for each curvature was computed from the extracted data using Equation 4.23, and the bending moment per unit width was plotted against the applied curvature for the duration of the analysis.

4.4 Macro-scale modelling

The meso-mechanical RUC model presented in this study aims to capture the non-linear bending response of thin woven fibre composites, as described in previous chapters. This model serves as a foundation for optimizing structural components made from this material. The next step is to develop an efficient method for incorporating the observed stiffness variation into simulations of shell structures composed of thin woven fibre composites.

At the macro-mechanical modelling stage, this study seeks to simulate the bending response of a test coupon subjected to the column bending test, integrating the non-linear bending stiffness variation obtained from the meso-mechanical analysis. The simulation will be conducted using Abaqus Standard along with a user-defined subroutine to model the bending process.

The following sections describe the numerical model, the user-defined subroutine, and the methodology for calculating non-linear bending stiffness from stress-strain curves.

4.5 Numerical model of the column bending test

The column bending test was chosen as the macro-mechanical simulation in this multi-scale modelling study for several reasons. First, it is straightforward to model, involving fewer numerical complexities, making it well-suited for testing a new numerical approach. Secondly, the model parameters can be adjusted to replicate the exact geometry of the experimental setup, allowing for a comparative study with the previously obtained experimental results. Modelling of the CBT has two aspects in this case. The geometry of the coupon and the type of elements is the first consideration. The other aspect is the rigid arms and the boundary conditions.

The test coupon between the rigid arms in the CBT is modelled with reduced integration four noded shell elements S4R. Reduced integration elements are selected to avoid the possibility of volumetric locking during the bending. The clamped region of the coupon is neglected in this model since it does not carry a moment during the test. The general shell stiffness section definition was assigned to the coupon geometry and initial section stiffness was defined in the ABAQUS user interface. The direct definition of the section stiffness instead of material properties gives the flexibility to incorporate a non-linear ABD stiffness matrix to the model using a user-defined subroutine such as User Defined GENeral Shell Section (UGENS) [54]. The initial ABD stiffness matrix was obtained from the linear analysis of the representative unit cell model described in section 4.2.4. Due to the simple geometry, the model is not sensitive to the mesh density. Hence a coarser mesh is chosen in order to reduce the computational time and problem complexity.

The pinned ends of the test setup are represented by two reference points, as shown in Figure 4.6. These reference points are positioned equidistant from the centre of the specimen, with the distance between the pinned connection and the specimen's centre set according to experimental values.

In the CBT, the bottom pinned connection remains fixed in all displacement directions, meaning the bottom reference point has no translational degrees of freedom (DOFs). However, it allows rotational motion around the x-axis. Conversely, the top pinned end moves downward along with the loading head while also rotating around the x-axis. Therefore, the top reference point permits displacement along the y-axis and rotation around the x-axis.

To apply the load, a prescribed displacement in the y-direction is assigned to the top reference point. Kinematic couplings with all DOFs fixed are used to model the rigid arms, ensuring that the applied vertical displacement is effectively transferred into rotational motion.

First, a simulation using the constant ABD stiffness matrix (Initial stiffness matrix) was conducted to obtain the moment-curvature relationship in the mid-region of the model, where the highest bending moment occurs. This region also corresponds to where the DIC curvature measurement is recorded. The objective was to determine whether any geometrically non-linear bending response arises in the coupon due to the test configuration.

Figure 5.8 illustrates the moment-curvature response obtained from the simulation with a constant section stiffness matrix. Subsequently, the bending stiffness variation was incorporated into the model using a UGENS subroutine, with the methodology detailed in the next section.

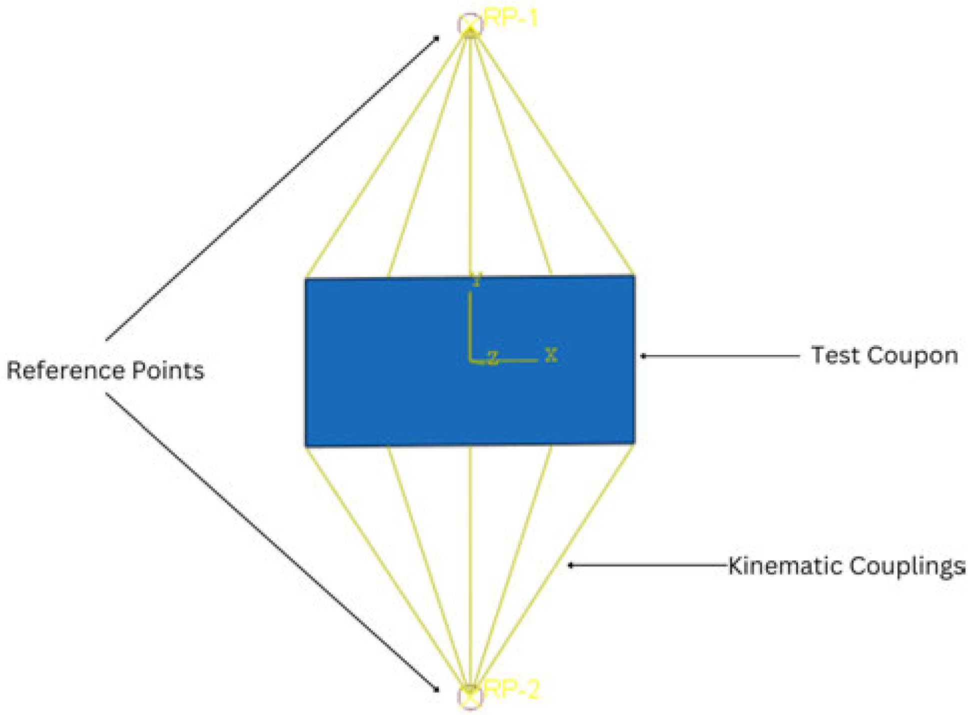

Fig. 4.6 CBT model in Abaqus CAE

4.6 Implementation of the user-defined subroutine

The Abaqus UGENS subroutine is used to modify the mechanical behaviour of shell elements in terms of generalised quantities. Essentially, it allows the definition of relationships between strain and generalised forces for each load increment, as shown in Equation 4.24.

The subroutine is fed with the current and next strain values of each element in every increment and it can derive the stiffness entries based on these field variables when the corresponding forces or stiffnesses to those variables are inserted in the subroutine. Therefore, in this study, we input the Strain and corresponding stiffness curves into the subroutine to adjust the stiffness of each shell element.

For each finite element iteration, the strain components of every shell element are mapped onto the stiffness curves to determine the corresponding equivalent stiffness matrix. The updated forces and moments are then calculated at the end of the increment.

In the subroutine presented here, only the stiffness curve for the D_{11} component of the section stiffness matrix is updated, as the primary objective of this study is to capture the non-linearity in the bending response of the material. To maintain the symmetry of the section stiffness matrix, the D_{22} component is constrained to match the value of D_{11}.

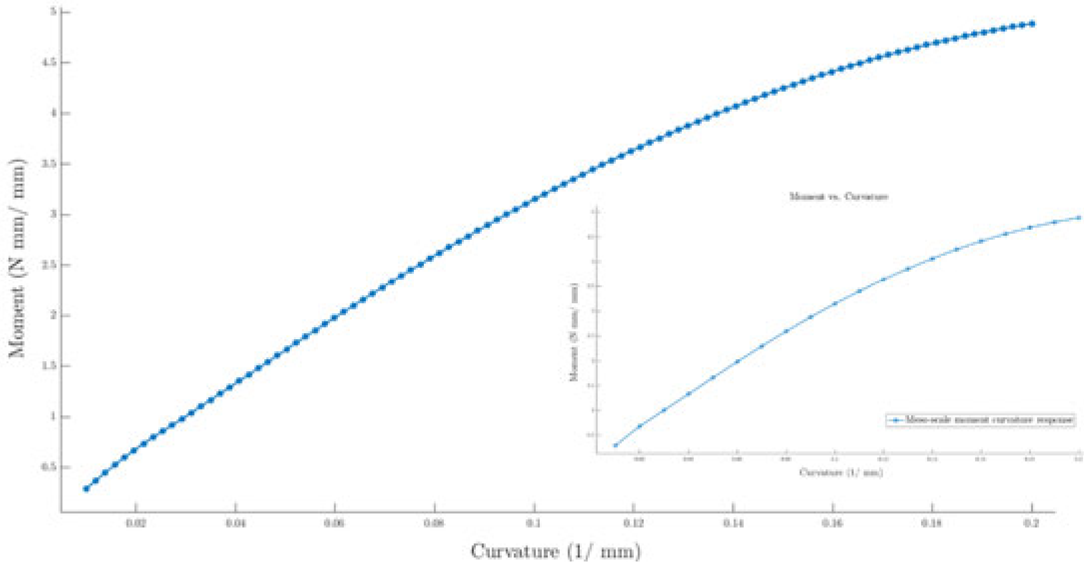

Fig. 4.7 Interpolated strain points from the original points of the moment-curvature response

$$(N_i, M_i) = \{[A], [B], [C], [D]\}_{ij,\mathrm{RUC}}(\varepsilon_j, \kappa_j), \tag{4.24}$$

4.6.1 Stiffness curves input in the user subroutine

The stiffness curves (the moment vs. Curvature plots) are interpolated into pre-defined strain points for code input. In the study, a hundred strain points were used and the stiffness curves are then smoothed using a polynomial curve fitting function in order to prevent swift changes in the stiffness values in the subroutine. The number of strain points used in the study is considered sufficient to describe the original stiffness of the material. The stiffness curves before and after smoothing are shown in the Figures 4.7 and 4.8.

These stiffness curve data are essentially related only to D_{11} hence a pure bending moment is applied to the meso-model. Then all stiffness points are input into the algorithm as two arrays, one containing the strain values and the other containing the corresponding stiffness values. The code then creates stiffness and strain three-dimensional arrays. In both arrays, the first index is the ID; we define ID as a counter running from one to the number of strain points. The second and third indices define the components in the 6x6 stiffness matrix. Therefore, the indexes only relevant to D_{11} are updated while keeping the other components constant. After the assembly, the stiffness 3D array and the strain 3D array will have one-to-one pairing provided that ID is the key for obtaining the pairs from the arrays.

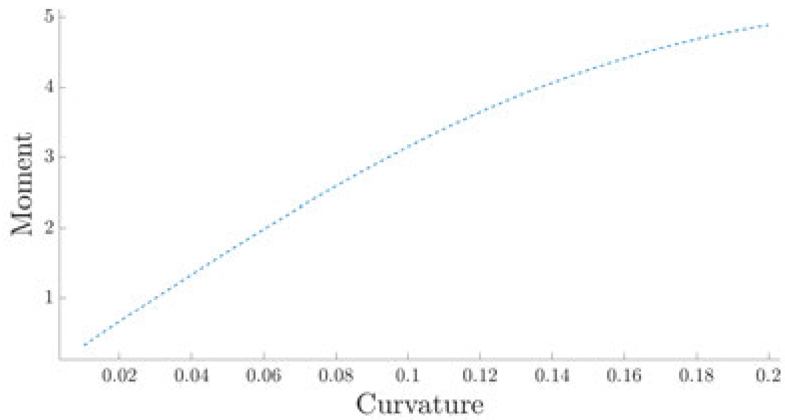

Fig. 4.8 Smoothed bending response from the meso-scale study

4.6.2 Updating the section forces

At each FE iteration, UGENS collects the strain values at the current time and the strain increment. Based on these values it can locate the corresponding strain value in the strain array. Based on the location identifier, a stiffness matrix can be assembled from the input stiffness values. A linear interpolation is done when the strain values fall out of the range of defined strain values. Based on the total strain and the new stiffness, the new force values can be calculated for the next increment.

4.6.3 State variable update

No other state variables are updated except the FORCE state variable. The initial Jacobian is defined using the initial stiffness matrix. The Jacobian only affects the convergence rate in this case and it is observed, that such approximation was adequate here. A modified Riks method is used to deal with the numerical instabilities. It modifies the integration method with an additional load proportionality factor. It is common to observe convergence difficulties if dramatic changes in mechanical properties are present between the steps or the adjacent elements. Therefore some numerical adjustments are made for the problem, such as decreasing the maximum load step, smoothing the stiffness curves as presented before, and relaxing the convergence parameters.

After performing the simulation with the non-linear bending stiffness variation, the moment-curvature behaviour of the mid-section of the specimen is extracted. The final coupon deformation is shown in the Figure 4.9.

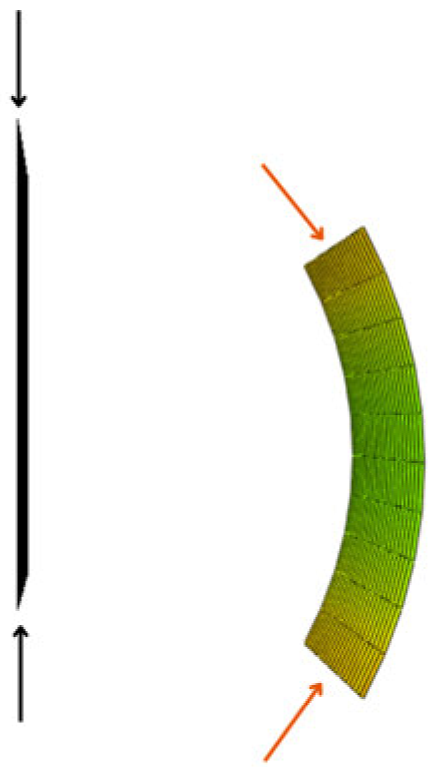

Fig. 4.9 Deformation snapshot of the test coupon from the simulation

Chapter 5

Results and Discussion

This chapter evaluates the effectiveness of the characterisation methods used in CBT analyses and examines the moment-curvature response obtained from the Column Bending Test, comparing it with predictions from the numerical multi-scale models.

5.1 Comparison of CBT analysis methods

This study used three approaches to analyze the experimental readings from the column bending test. Firstly, a simple geometric solution was employed due to its simplicity, despite the assumptions used in its formulation. As shown in Figure 5.1, the moment-curvature response for the material obtained from this method of analysis follows a linear path. However, it shows a slight reduction in bending stiffness at high curvatures, which is less pronounced compared to the observations made by Mallikarachchi and Pellegrino [19]. Two factors could contribute to deviations from the simplified geometric analysis: first, the presence of material non-linearities, and second, the presence of a non-constant bending moment along the arc length of the specimen.

To examine the significance of the effect of material non-linearity, the second error factor was first investigated using the theory of Elastica. Elastica theory enables accurate modelling of the large deflection of slender elements without relying on the constant curvature assumption used in geometric analysis. The Elastica analysis of the test, shown in Figure 5.2, reveals no significant difference from the geometric analysis. This observation suggests that the second assumption of the simple geometric analysis, the constant curvature assumption, is practically accurate.

Therefore, significant non-linearity in the bending response could not be observed using either geometrical assumptions or the Elastica partial differential solution. According to Sharma et al. [1], both methods deviate from realistic results when significant material

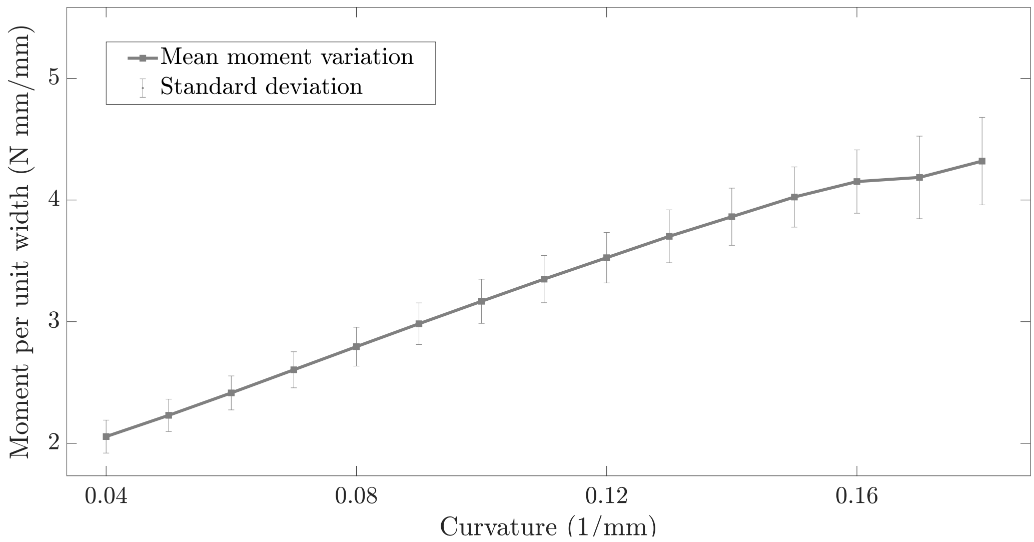

Fig. 5.1 Moment-curvature response of a two-ply plain weave laminate calculated using the geometric solution.

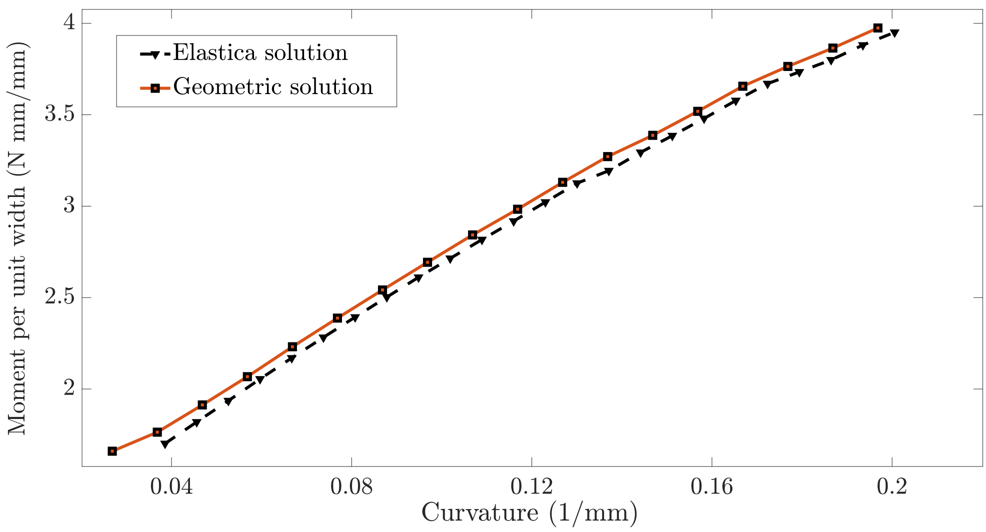

Fig. 5.2 Moment-curvature response obtained from simplified geometry and Elastica methods for the PW-SP3 specimen.

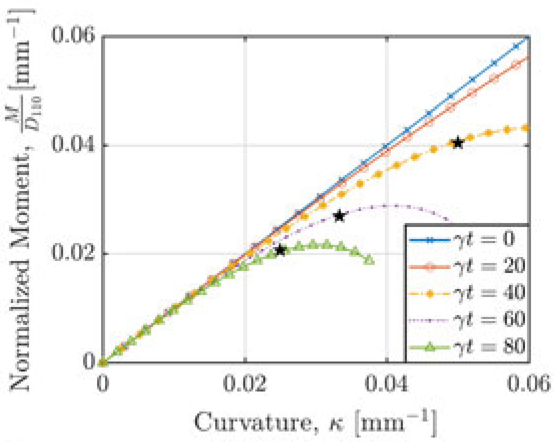

Fig. 5.3 Normalised moment against the curvatures as a function of the non-linear parameter [1]

non-linearities are present. To address this, they introduced a non-linearity factor that can be incorporated into calculations to achieve a more accurate representation of the material's bending response under pure bending. As this factor increases, the non-linearity in the bending response becomes more pronounced, as shown in Figure 5.3. The objective of this experimental study is to characterise the bending response of the material using a purely experimental approach, without making prior assumptions about the laminate's material properties. Therefore, the authors did not extract non-linearity factors from the literature to construct the bending response using the aforementioned analytical methods. Instead, direct experimental readings from DIC were used to capture the material's bending response. Figure 5.4 illustrates the bending response of the laminate obtained from direct DIC readings, clearly demonstrating a significant non-linear response.

The reduction in bending stiffness, compared to the extrapolated bending stiffness, is around 28%, which is comparable to the 20% reduction observed by Mallikarachchi and Pellegrino, despite their use of a different resin in their two-ply laminate (HexPly913).

With these results, an inverse calculation technique can be used to determine the non-linearity parameter and incorporate it into the geometrical analysis and Elastica solution. This approach would allow for predicting the bending response of the laminate without relying on the DIC technique, using only simple readings from a universal testing machine. This presents a potential direction for future research to validate the solution of the whole analysis.

Therefore, we conclude that the analysis methods used for the CBT are only accurate when material non-linearity factors are considered. Relying solely on geometrical non-linearities can lead to inaccurate results.

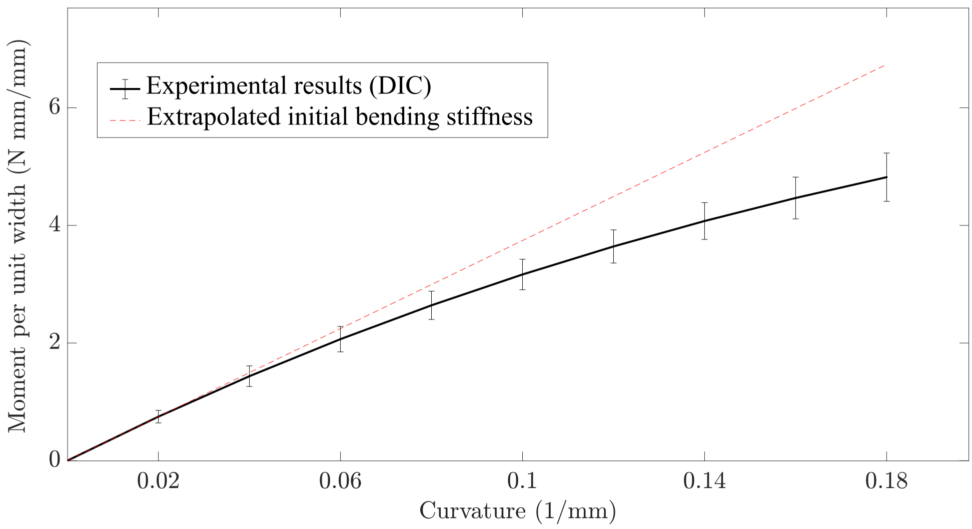

Fig. 5.4 Moment-curvature response of the PW-SP3 specimen obtained with direct DIC measurements, showing stiffness reduction with increasing curvature.

5.2 Comparison of numerical results

5.2.1 Meso-mechanical moment-curvature response analysis

This section compares the bending response obtained from the experimental analysis and compares it with the results obtained from the meso-mechanical model presented in this study. As demonstrated in Figure 5.4, the experimental results from the CBT show a clear bending stiffness reduction as the curvature increases, while former studies are based on two different tests. Figure 5.5 compares the moment-curvature response obtained from the numerical model with non-linear geometric analysis against the experimental results. A numerical model with cohesive interactions is successful in capturing the reduction of bending stiffness obtained during the experiments and lies within the standard deviation obtained from the different tests. However, the predictions tend to predict higher moments at higher curvatures beyond 0.08 mm^{-1} compared to the experimental moment-curvature envelope.

A detailed analysis of separation along cohesive surfaces reveals a relative slip between the tows in the direction of the applied moment. This micro-slip between tows contributes to a reduction in stiffness. As illustrated in Figure 5.5, the numerical model with tie constraints does not exhibit any stiffness reduction. It is important to note that the only difference between the two models lies in the interaction modelling approach: one utilizes tie constraints to bind the tows, while the other allows tow separation through cohesive interactions.

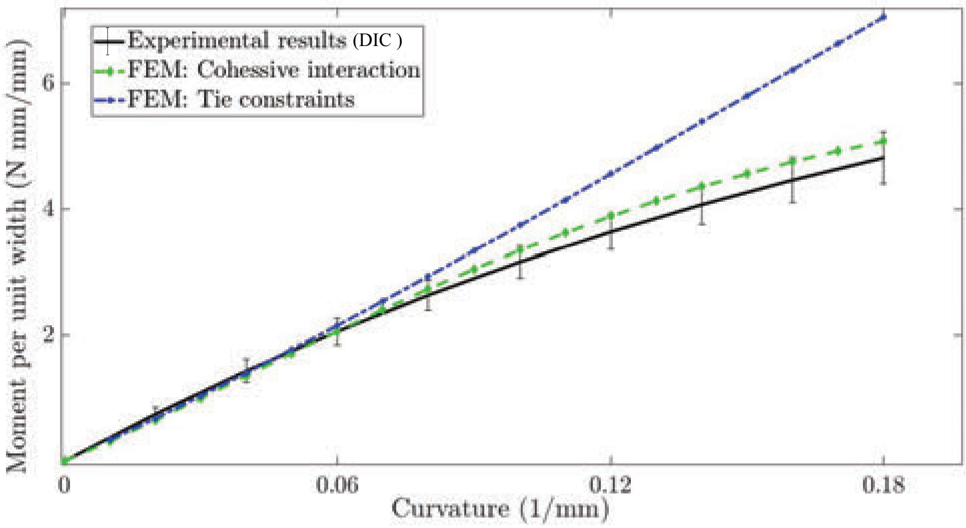

Fig. 5.5 Comparison of moment-curvature response obtained from numerical models with rigid tie constraints and cohesive interactions between the tows against the experimental results.

The moment-curvature response obtained from the numerical model with a non-linear elastic constitutive law for tows is compared with the numerical model with the linear elastic constitutive law and the experimental results in the Figure 5.6

Unlike in the model with tie constraints, both models allow for tow separations through cohesive interaction in this case. It is important to note that the results from the new material model closely align with the mean experimental response with increasing curvature. This implies that the non-linear geometric deformation of tows plays a critical role in the bending stiffness variation of the laminate.

Both models are within the standard deviation observed in the experimental study. The model with non-linear constitutive law for tows is more closely aligned with the experimental results providing much greater accuracy. As seen from both the experimental analysis of the CBT and the numerical analysis, we can conclude that material non-linearity is a critical aspect when predicting the bending response.

5.2.2 Macro-mechanical moment-curvature response analysis

This section discusses the results obtained from the numerical simulation of the CBT and compares them with the experimental results and the meso-mechanical bending response.

Figure 5.7 shows the section curvature distribution in the simulated coupon. The curvature distribution is almost uniform in the coupon and the maximum curvature is obtained at the

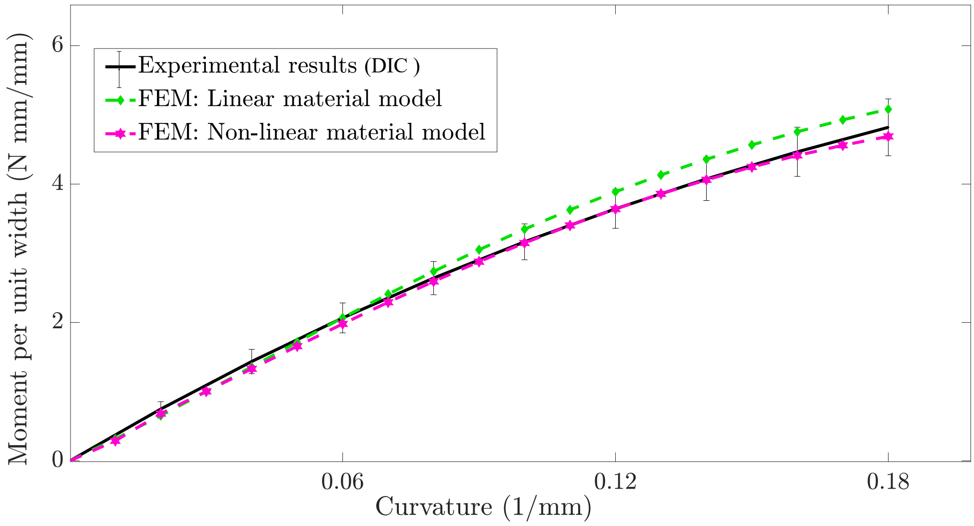

Fig. 5.6 Comparison of moment-curvature responses obtained from the numerical model with cohesive interaction considering with and without non-linear tows against the experimental results.

mid-depth of the coupon. The moment and curvature readings from the mid-region of the coupon were extracted and plotted as shown in Figure 5.7 for both linear and non-linear section models.

The numerical model of the CBT with a constant section stiffness does not exhibit a stiffness reduction with increasing curvature and follows a linear path which coincides with the extrapolated initial bending stiffness. This result leads to the conclusion that the test geometry does not impose any geometric non-linearity into the material bending response. The numerical model with the non-linear section stiffness was able to capture moment-

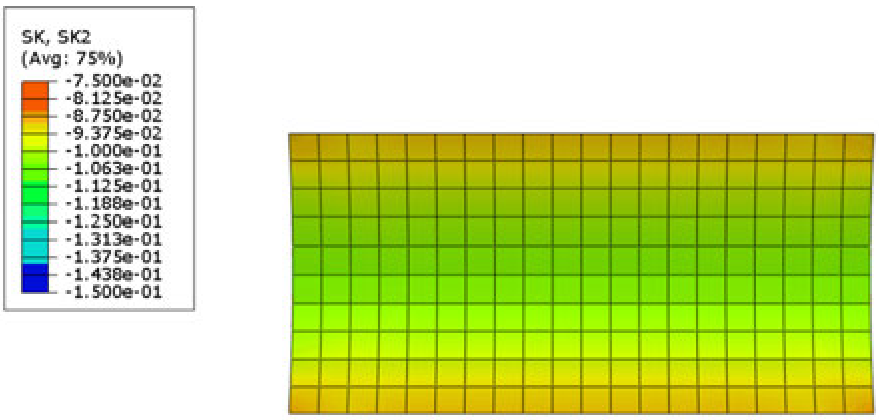

Fig. 5.7 Curvature variation along the length of the coupon

curvature response approximately up to 0.17 1/mm and the envelope follows the same path of the bending response from the RUC model with a non-linear material model.

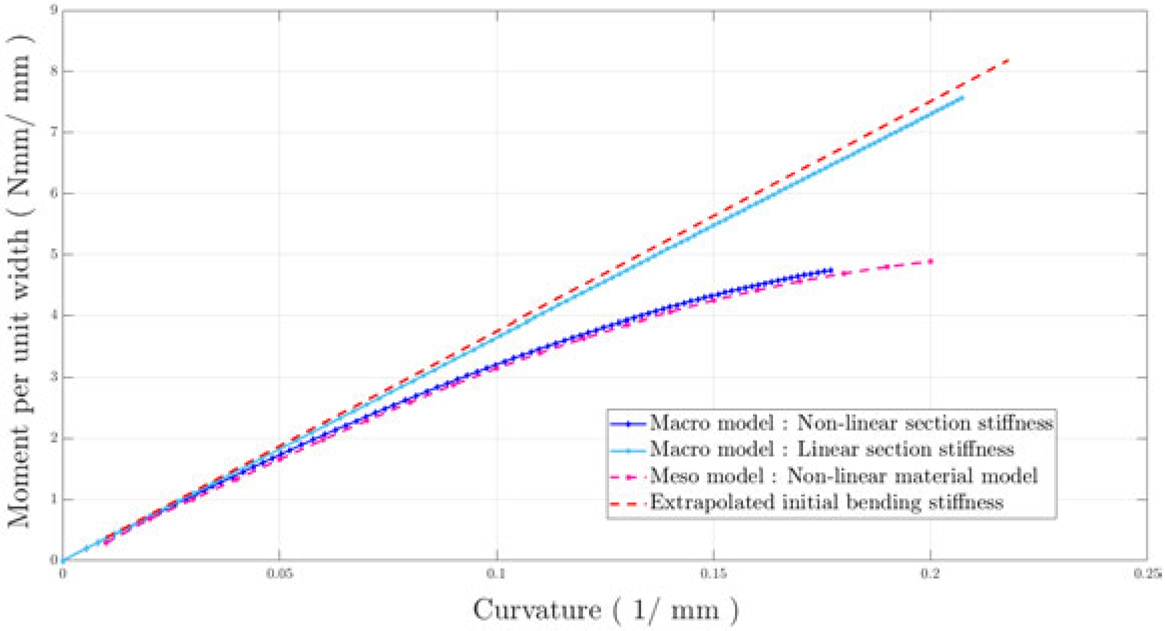

Fig. 5.8 Comparison of moment-curvature responses obtained from the CBT simulations with linear and non-linear section stiffnesses against the response obtained from the meso-mechanical model with a non-linear material model

These results lead to the conclusion that incorporating the non-linear section stiffness can yield accurate bending response in the macro-scale and the method provides a feasible way to simulate even more complex structures made from the material. Since we can observe a significant reduction in the macro-scale simulations, this comprehensive methodology provides a streamlined process to optimize future thin-walled space structures as well.

Chapter 6

Conclusions and Future Work

6.1 Conclusions

Understanding the flexural behaviour of thin woven fibre composites is crucial for designing weight-sensitive structures. The reduction in bending stiffness at high curvatures has been a longstanding question in this field. Although this phenomenon has been observed in physical testing, a comprehensive explanation was previously lacking, limiting the effective use of simulations in the design process. This study presents a combined experimental and multi-scale numerical modelling approach to address this issue.

Previous experimental studies on the flexural behaviour of thin woven carbon fibre composites were unable to capture the full non-linear response. In this study, the CBT was employed to characterise the fully non-linear behaviour of the laminate, as it generates a nearly uniform pure bending moment throughout the specimen. To derive moment-curvature plots from displacement and force measurements, the author applied both simple geometric analysis and Euler's elastica analysis. These methods provided an upper-bound solution for the bending response, as they assume a linear material model. While the incorporation of a non-linear parameter would resolve this limitation, this study instead utilized direct DIC measurements to construct an experimentally validated moment-curvature response. The results indicate a stiffness reduction of approximately 28% at failure, consistent with previous findings in the literature.

Previous numerical studies aimed at capturing the non-linear bending response of thin woven fibre composites lacked two key aspects in their models. First, the relative motion between tows was not accurately represented. Second, the material nonlinearity of the tows—arising from the inherent behaviour of the fibres—was not incorporated into the tow material model.

The meso scale numerical model utilised in this study addresses these limitations by introducing cohesive interactions between the tows and employing a strain-dependent material model for the tow material. The model reveals that the combined effects of tow and ply relative motion, along with tow material nonlinearity, play a critical role in the bending behaviour of the laminate.

The proposed model accurately captures the bending response and shows strong agreement with experimental results. This numerical approach is thus applicable to various layup configurations of thin woven composites, potentially reducing the need for costly and time-consuming experimental investigations—a significant advancement in the field.

Furthermore, a methodology was introduced to incorporate non-linear bending stiffness into macro-scale structures composed of the laminate. The bending behaviour of the CBT coupon was simulated using ABAQUS Standard, comparing two models: one with constant section stiffness and another with non-linear section stiffness. The latter showed excellent agreement with both experimental and meso-scale numerical results, as illustrated in Figure 5.8. The proposed framework for macro-scale modelling is straightforward and can be applied to a wide range of structural simulations. However, numerical adjustments, such as modifications to convergence parameters, may be required for specific applications. This study provides a robust foundation for integrating non-linear flexural behaviour into the design and analysis of composite structures.

6.2 Recommended Future Works

The following are a few suggestions for future research directions.

1. Generalising the simple geometric approach and the Elastica solution for CBT analysis by calculating the non-linear parameter

2. Application of the proposed macro-scale simulation framework for deployable boom structures to observe the deployment kinematics

3. Conduct a sensitivity analysis on meso-scale RUC model to quantify the driving factors of non-linear bending behaviour.

References

[1] Ajay Sharma, Thomas Rose, Nicholas Bearns, Thomas Murphey, and Francisco Lopez Jimenez. Analysis of geometric and material nonlinearity in the column bending test. *AIAA Journal*, 62:1–11, 12 2023.

[2] Sergio Pellegrino. *Elastic Folding of Shell Structures*, pages 77–98. 01 2001.

[3] Joni Jorgensen, Ehlias Louis, Jason Hinkle, Mark Silver, Bill Zuckermandel, and Scott Enger. Dynamics of an elastically deployable solar array: Ground test model validation. *Collection of Technical Papers - AIAA/ASME/ASCE/AHS/ASC Structures, Structural Dynamics and Materials Conference*, 3, 04 2005.

[4] D. S. Adams and M. Mobrem. Lenticular jointed antenna deployment anomaly and resolution onboard the mars express spacecraft. *Journal of Spacecraft and Rockets*, 46(2):403–410, 2009.

[5] Rui Cai and Tan Jin. The effect of microstructure of unidirectional fibre-reinforced composites on mechanical properties under transverse loading: A review. *Journal of Reinforced Plastics and Composites*, 37(22):1360–1377, 2018.

[6] A. P. Mouritz, M. K. Bannister, P. J. Falzon, and K. H. Leong. Review of applications for advanced three-dimensional fibre textile composites. *Composites Part A: Applied Science and Manufacturing*, 30:1445–1461, 1999.

[7] Y. Huang, X. Tian, Z. Zheng, D. Li, A. V. Malakhov, and A. N. Polilov. Multiscale concurrent design and 3d printing of continuous fiber reinforced thermoplastic composites with optimized fiber trajectory and topological structure. *Composite Structures*, 285:115241, 2022.

[8] Tian-Wei Liu, Jiang-Bo Bai, Nicholas Fantuzzi, and Xiang Zhang. Thin-walled deployable composite structures: A review. *Progress in Aerospace Sciences*, 146:100985, 2024.

[9] William K. Wilkie. *Overview of the NASA Advanced Composite Solar Sail System (ACS3) Technology Demonstration Project.*

[10] O. Soykasap. Micromechanical models for bending behavior of woven composites. *Journal of Spacecraft and Rockets*, 43(5):1093–1100, 2006.

[11] A. D. B. L. Ferreira, P. R. O. Novoa, and A. T. Marques. Multifunctional material systems: A state-of-the-art review. *Composite Structures*, 151:3–35, 2016.

[12] C. Mallikarachchi and S. Pellegrino. Design and validation of thin-walled composite deployable booms with tape-spring hinges. In *Proceedings of an unspecified conference*, s.l., 2011. s.n.

[13] H. M. Y. C. Mallikarachchi and S. Pellegrino. Failure criterion for two-ply plain weave cfrp laminates. *Journal of Composite Materials*, 47(11):1357–1375, May 2013.

[14] M. Y. Hamillage and H. M. Y. C. Mallikarachchi. Predicting non-linear bending behaviour of thin woven fibre composites. In *Proceedings of [Conference Name]*, s.l., 2017. s.n.

[15] M. Jayasekara. *Non-linear Bending Behaviour of Thin Woven Fibre Composites Under High Curvatures*. PhD thesis, University of Moratuwa, s.l., 2020.

[16] Uditha Weerasinghe, Sumudu Herath, and Chinthaka Mallikarachchi. Homogenization of ultra thin woven composite structures at high curvatures. In *Proceedings of the Moratuwa Engineering Research Conference (MERCon)*, pages 1–5, 2022.

[17] M. Mobrem and D. Adams. Deployment analysis of the lenticular jointed antennas onboard the mars express spacecraft. *Journal of Spacecraft and Rockets*, 46(2):394–402, Mar. 2006.

[18] M. Sakovsky and S. Pellegrino. Closed cross-section dual-matrix composite hinge for deployable structures. *Composite Structures*, 208:784–795, Oct. 2018.

[19] H. M. Y. C. Mallikarachchi and S. Pellegrino. Simulation of quasi-static folding and deployment of ultra-thin composite structures. In *49th AIAA/ASME/ASCE/AHS/ASC Structures, Structural Dynamics, and Materials Conference*, 2008.

[20] Maria Sakovsky, Sergio Pellegrino, and H.M.Y.C. Mallikarachchi. *Folding and Deployment of Closed Cross-Section Dual-Matrix Composite Booms*.

[21] H. M. Y. C. Mallikarachchi. *Thin-walled composite deployable booms with tapespring hinges*. PhD thesis, University of Cambridge, May 2011.

[22] K. Ubamanyu and H. M. Y. C. Mallikarachchi. Simulation of dual-matrix composite booms. In *Proceedings of the Annual Sessions of Society of Structural Engineers*, 2016.

[23] T. W. Murphey, W. Francis, B. Davis, and J. M. Mejia-Ariza. High strain composites. In *2nd AIAA Spacecraft Structures Conference*, 2015.

[24] Jifeng Gao, Wujun Chen, Bing Yu, Pengxuan Fan, Bing Zhao, Jianhui Hu, Daxu Zhang, Guangqiang Fang, and Fujun Peng. A multi-scale method for predicting abd stiffness matrix of single-ply weave-reinforced composite. *Composite Structures*, 230:111478, 2019.

[25] Jeffrey Yee and Sergio Pellegrino. *Biaxial Bending Failure Locus for Woven-Thin-Ply Carbon Fibre Reinforced Plastic Structures*.

[26] G. E. Sanford, E. V. Ardelean, T. W. Murphey, and M. M. Grigoriev. High strain test method for thin composite laminates. In *16th International Conference on Composite Materials (ICCS-16)*, Porto, Portugal, June 28–30 2011.

[27] M. E. Peterson and T. W. Murphey. High strain flexural characterization of thin cfrp unidirectional composite lamina. In *31st American Society for Composites Technical Conference*, Williamsburg, Virginia, September 19–22 2016.

[28] M. E. Peterson and T. W. Murphey. Large deformation bending of thin composite tape spring laminates. In *54th AIAA Structures, Structural Dynamics, and Materials Conference*, Boston, Massachusetts, April 8–11 2013.

[29] J. C. H. Yee and S. Pellegrino. Folding of woven composite structures. *Composites Part A: Applied Science and Manufacturing*, 36:273–278, 2005.

[30] F. Lopez Jimenez. *Mechanics of Thin Carbon Fiber Composites with a Silicone Matrix*. PhD thesis, California Institute of Technology, Pasadena, California, 2011.

[31] Juan M Fernandez and Thomas W Murphey. A simple test method for large deformation bending of thin high strain composite flexures. In *2018 AIAA spacecraft structures conference*, page 0942, 2018.

[32] Ajay Sharma, Riley Perez, Nicholas Bearns, Thomas Rose, and Francisco Lopez Jimenez. Some considerations involving testing guidelines for large curvature bending of high strain composites using the column bending test. 01 2021.

[33] Ajay Sharma, Thomas Rose, Andrew Seamone, Thomas Murphey, and Francisco Lopez Jimenez. Analysis of the column bending test for large curvature bending of high strain composites. 01 2019.

[34] A. J. Lee and J. M. Fernandez. Mechanics of bistable two-shelled composite booms. In *5th AIAA Spacecraft Structures Conference, AIAA Scitech 2018 Forum*, Kissimmee, FL, January 8–12 2018.

[35] J. M. Fernandez et al. Nasa's advanced solar sail propulsion system for low-cost deep space exploration and science missions that use high performance rollable composite booms. In *4th International Symposium on Solar Sailing*, Kyoto, Japan, January 17–20 2017.

[36] J. M. Fernandez. Advanced deployable shell-based composite booms for small satellite applications including solar sails. In *4th International Symposium on Solar Sailing*, Kyoto, Japan, January 17–20 2017.

[37] J. M. Fernandez et al. An advanced composites-based solar sail system for interplanetary small satellite missions. In *5th AIAA Spacecraft Structures Conference, AIAA Scitech 2018 Forum*, Kissimmee, FL, January 8–12 2018.

[38] Gao Jifeng, Wu-jun Chen, J. Chen, J. Hu, Bing Zhao, Daxu Zhang, G. Fang, and Fujun Peng. Accuracy analysis on counterweight-balanced column bending test. *Experimental Mechanics*, 62, 09 2021.

[39] J. I. Múgica et al. Multiscale modelling of thermoplastic woven fabric composites: From micromechanics to meso mechanics. *Composite Structures*, 20, August 2019.

[40] J. Mao et al. A modeling approach across length scales for progressive failure analysis of woven composites. *Applied Composite Materials*, 20:213–231, June 2013.

[41] R. M. Jones. *Mechanics of Composite Materials*. Taylor & Francis Inc., 2nd edition, 1999.

[42] Inc. Correlated Solutions. *Vic-3D Testing Guide*.

[43] Thomas Murphey, Gregory Sanford, and Mikle Grigoriev. Nonlinear elastic constitutive modelling of large strains in thin carbon fibre composite flexures. In *16th International conference on composite structures, Porto, Portugal*, 2011.

[44] Torayca. *Technical Data Sheet No. CFA-001, T300 Data Sheet*. Toray Industries, Inc.

[45] PATZ. *Technical Data Sheet PMT-F4*. PATZ Materials and Technologies.

[46] M. Daniel and O. Ishai. *Engineering Mechanics of Composite Materials*. McGraw-Hill Book Company, 2nd edition, 2006.

[47] S. C. Quek, A. M. Waas, K. W. Shahwan, and V. Agaram. Analysis of 2d triaxial flat braided textile composites. *International Journal of Mechanical Sciences*, 45(6):1077–1096, 2003. [Online].

[48] G. Curtis, J. Milne, and W. Reynolds. Non-hookean behaviour of strong carbon fibres. *Nature*, 220(5171):1024–1025, 1968.

[49] Uba K. Ubamanyu and Sergio Pellegrino. *Nonlinear Behavior of IM7 Carbon Fibers in Compression Leads to Bending Nonlinearity of High-Strain Composites*, page Art. No. 2023–0580. American Institute of Aeronautics and Astronautics, Jan 2023. Funding by Space Solar Power Project.

[50] A. Schlothauer, G. A. Pappas, and P. Ermanni. Material response and failure of highly deformable carbon fiber composite shells. *Composites Science and Technology*, 199:108378, October 2020.

[51] Wim H.M. Van Dreumel and John L.M. Kamp. Non hookean behaviour in the fibre direction of carbon-fibre composites and the influence of fibre waviness on the tensile properties. *Journal of Composite Materials*, 11(4):461–469, 1977.

[52] V. Keryvin, A. Marchandise, and J.-C. Grandidier. Non-linear elastic longitudinal behaviour of continuous carbon fibres/epoxy matrix composite laminae: Material or geometrical feature? *Composites Part B: Engineering*, 247:110329, 2022.

[53] Nishangani Gowrikanthan, Milindu Jayasekara, Chinthaka Mallikarachchi, and Sumudu Herath. Effects of tow arrangements on the homogenized response of carbon fiber woven composites. *Composite Structures*, 300:116081, 2022.

[54] Michael Smith. *ABAQUS/Standard User's Manual, Version 6.9*. Dassault Systèmes Simulia Corp, United States, 2009.

[55] H.M.Y.C. Mallikarachchi. Predicting mechanical properties of thin woven carbon fiber reinforced laminates. *Thin-Walled Structures*, 135:297–305, 2019.

[56] H. Wijesuriya. Predicting non-linear bending behaviour of ultra-thin woven fibre composites. Master's thesis, University of Moratuwa, Sri Lanka, 2019.

APPENDIX A

Geometric analysis of the column bending test

```
%% import matrices to the workspace

for i = 1:numel(K_Matrix)
    % Create variable name based on index
    variableNameM = sprintf('M_%d', i);
    variableNameK = sprintf('K_%d', i);

    % Assign matrix to variable
    eval([variableNameM ' = M_Matrix{i};']);
    eval([variableNameK ' = K_Matrix{i};']);
end

%% Geometric analysis
folder1 = 'E:\CBT Experimental
data\Matlab\CBT\2019_12_17\DIC';
folder = 'E:\CBT Experimental
data\Matlab\CBT\2019_12_17\Instron';
l_s1 =[10,10,10,10,10, 11, 11, 11, 11, 11, 11];
w1 = [20.33, 20.30, 20.27, 20.70, 20.00, 20.81, 20.28,
20.48, 18.34, 20.56, 21.08];
K_Matrix={};
M_Matrix={};
DeltaP={};


Force_M={};
Delta_p={};
% Loop through each file
for i = 1:11

    % Generate the file name
    filename = sprintf('CBTD90_12172019_Failure_%d.csv',
i);

    % Read the data from the CSV file
    filepath = fullfile(folder, filename);
%     data = csvread(filepath); % or use readtable if you
want to preserve column headers
```

```
    startRow = 16;
    endRow = 'end';  % To read until the end of the sheet
    columnsToRead = 'A:C';
    data = xlsread(filepath, columnsToRead,
sprintf('A%d:%s', startRow, endRow));



    Time1 = data(:, 1);
    time=Time1(~isnan(Time1));
    delta1 = data(:, 2);
    delta= delta1(~isnan(delta1)) ;
    DeltaP{end+1}=delta;

    p1 = data(:, 3);
    p= p1(~isnan(p1));
    %specimen free length and width
    l_s = l_s1(i);
    w = w1(i);

%calculation of initial angle of eccentricity; theta
    l_1= 28; Delta_x=0;

    l = sqrt(l_1^2 + Delta_x^2);
    theta = - atan(Delta_x/l_1);


    ph=[];
    r=[];

% calculate initial phi and r
    fun1 = @(phi) delta(1) - l_s + 2*l_s/phi*sin(phi/2) -
2*l*(cos(theta)-cos(theta + phi/2));
    ph(1) = fzero(fun1 ,eps);
    r(1) = l*sin(theta+0.5*ph(1))+l_s/ph(1)*(1-
cos(0.5*ph(1)));

% calculate phi and r for each increment
    for ii=2:length(delta)
        fun = @(phi) delta(ii) - l_s + 2*l_s/phi*sin(phi/2)
- 2*l*(cos(theta)-cos(theta + phi/2));
        ph(ii) = fzero(fun ,ph(ii-1));
        r(ii) = l*sin(theta+0.5*ph(ii)) + l_s/ph(ii)*(1-
cos(0.5*ph(ii)));
```

```
    end

% Calculation of Moment and Curvature
    M = - ((p).*(transpose(r)+5))/w;
    K = - transpose(ph)./l_s;
    K_Matrix{end+1}=K;
    M_Matrix{end+1}=M;
    plot(K,M,'.')
    hold on

end


%% mean plot
y_all=[];
for x = 1:11
    y=M_Matrix{1,i};
    y_all=[y_all;y];

end

%% new cal
folder1 = 'E:\CBT Experimental
data\Matlab\CBT\2019_12_17\DIC';
folder = 'E:\CBT Experimental
data\Matlab\CBT\2019_12_17\Instron';
l_s1 =[10,10,10,10,10, 11, 11, 11, 11, 11, 11];
w1 = [20.33, 20.30, 20.27, 20.70, 20.00, 20.81, 20.28,
20.48, 18.34, 20.56, 21.08];
K_Matrix={};
M_Matrix={};

for i = 1:11

    % Generate the file name
    filename = sprintf('CBTD90_12172019_Failure_%d.csv',
i);

    % Read the data from the CSV file
    filepath = fullfile(folder, filename);
%     data = csvread(filepath); % or use readtable if you
want to preserve column headers
```

```
    startRow = 16;
    endRow = 'end';  % To read until the end of the sheet
    columnsToRead = 'A:C';
    data = xlsread(filepath, columnsToRead,
sprintf('A%d:%s', startRow, endRow));

    delta1 = data(:, 2);
    delta= delta1(~isnan(delta1)) ;
    p1 = data(:, 3);
    p= p1(~isnan(p1));
    %specimen free length and width
    ls = l_s1(i);
    w = w1(i);

%calculation of initial angle of eccentricity; theta
    l= 28.39;
    alpha=0.00000001;
    gamma=[];
    r=[];
    theta=atan(4.7/28);

    fun2= @(gamma)
2*l*cos(alpha+theta)+ls*sin(alpha)/alpha-
2*l*(cos(alpha+gamma+theta))-
ls*sin(alpha+gamma)/(alpha+gamma)-delta(1);
    gamma(1)=fzero(fun2 ,eps);
    r(1) =
l*sin(alpha+theta+gamma(1))+0.5*ls/(alpha+gamma(1))*(1-
cos(alpha+gamma(1)));

    for ii=2:length(delta)
        fun2= @(gamma)
2*l*cos(alpha+theta)+ls*sin(alpha)/alpha-
2*l*(cos(alpha+gamma+theta))-
ls*sin(alpha+gamma)/(alpha+gamma)-delta(ii);
        gamma(ii)=fzero(fun2 ,gamma(ii-1));
        r(ii) =
l*sin(alpha+theta+gamma(ii))+0.5*ls/(alpha+gamma(ii))*(1-
cos(alpha+gamma(ii)));

    end

    % Calculation of Moment and Curvature
    M = ((p).*(transpose(r)))/w;
```

```
    K = (transpose(2*gamma+2*alpha))./ls;
    if (i~=5 && i~=3 && i~=11)
        [Mm,id]=max(M);
        M=M(1:id);
        K=K(1:id);
        K_Matrix{end+1}=K;
        M_Matrix{end+1}=M;
    end
    plot(K,M,'.')
    hold on

end

%% plots

for i=1:11
    if ( i==3 )
        plot(K_Matrix{1,i}, M_Matrix{1,i});
    end
    hold on
end

%%

% Create a common K vector with 0.01 intervals
K_common = 0.04:0.01:max(cellfun(@max, K_Matrix));

% Initialize mean and standard deviation vectors
M_mean = zeros(size(K_common));
M_std = zeros(size(K_common));

% For each K value...
for i = 1:length(K_common)
    % Initialize a vector to hold the M values for this K
    M_values = [];

    % For each data set...
    for j = 1:length(M_Matrix)
        % Find the M values corresponding to the current K
        M_interp = interp1(K_Matrix{j}, M_Matrix{j},
K_common(i));

        % Only consider M values up to its maximum
        if M_interp <= max(M_Matrix{j})
```

```
            M_values = [M_values; M_interp];
        end
    end

    % Calculate the mean and standard deviation of the M
values
    M_mean(i) = nanmean(M_values);
    M_std(i) = nanstd(M_values);
end

% Plot the mean M values with error bars
figure;
plot(K_common, M_mean,'r','LineWidth', 1.5);
grid on
hold on
errorbar(K_common, M_mean, M_std,'r.');
xlabel('K');
ylabel('Mean M');
title('Mean M vs K with error bars');

hold on

% Calculate the standard deviation
std_y = std(y_all, 0, 1);

% Create a new x vector with increments of 0.02
x_new = min(x):0.02:max(x);

% Interpolate the mean_y and std_y values at the new x
points
mean_y_new = interp1(x, mean_y, x_new, 'linear');
std_y_new = interp1(x, std_y, x_new, 'linear');

% Plot the mean curve in black

plot(x_new, mean_y_new, 'k', 'LineWidth', 2);
grid on
hold on

% Add error bars in red
errorbar(x_new, mean_y_new, std_y_new, 'r.');

% Calculate the gradient of the mean_y vs x plot
gradient_y = gradient(mean_y_new, x_new);
```

```
% Plot a dashed line with the starting gradient of the
mean_y vs x plot in black
plot(x_new, gradient_y(1)*x_new, 'k--');

hold off

xlabel('Curvature');
ylabel('Bending Stiffness');
title('Moment vs Curvature (3rd Degree polynomial fit-Type
_ With 4.7 reduction)');
```

Elastica solution and the coupon shapes for the column bending test

```
% Constants
E = 145920;
I = 0.01804;
alpha_values = deg2rad(3:2:58); % convert to radians
gamma = deg2rad(9.528); % convert to radians
L = 28;
S =10;
figure;
hold on
pcr_all=[];
D_X=[];
D_Y=[];
M=[];
Kap=[];

% Initialize a cell array for the legend labels
legend_labels = cell(length(alpha_values), 1);
legend_handles = gobjects(length(alpha_values), 1); % For
storing plot handles

for i = 1:length(alpha_values)
    alpha = alpha_values(i);
    % Function for p
    p = @(theta, Pcr) sqrt(2*(Pcr/(E*I))*(cos(theta)-
cos(alpha)) + (Pcr*L*sin(gamma+alpha)/(E*I))^2);

    % Function for X and Y
    X = @(beta, Pcr) integral(@(theta) cos(theta)./p(theta,
Pcr), beta, alpha);
    Y = @(beta, Pcr) integral(@(theta) sin(theta)./p(theta,
Pcr), beta, alpha);

    % Function for S
    S_func = @(Pcr) integral(@(theta) 2./p(theta, Pcr), 0,
alpha) - S;

    % Solve for Pcr using fsolve
    Pcr_initial_guess = 1; % initial guess for Pcr
```

```
    Pcr = fsolve(S_func, Pcr_initial_guess); % solve for
Pcr
    pcr_all=[pcr_all,Pcr];

    % Generate beta values from 0 to alpha
    beta_values = linspace(0, alpha, 100);

    % Calculate X and Y for each beta
    X_values = arrayfun(@(beta) X(beta, Pcr), beta_values);
    Y_values = arrayfun(@(beta) Y(beta, Pcr), beta_values);

    % Create a mirror image of the curve by reflecting the
X values about the end point of the original curve
    X_mirror = 2*X_values(1) - X_values;

    % Concatenate the original and mirrored X and Y values
    X_combined = [X_values, X_mirror];%+L*cos(alpha+gamma);
    Y_combined = [Y_values, Y_values];%+L*sin(alpha+gamma);
% Y_values is the same for both curves
    X_combined = X_combined+L*cos(alpha+gamma);
    Y_combined = Y_combined+L*sin(alpha+gamma);
    XM=max(X_combined)+L*cos(alpha+gamma);
    D_X=[D_X,66-XM];
    D_Y=[D_Y,max(Y_combined)];
    M=[M,Pcr*max(Y_combined)/20.27];

    % Plot the combined curve in the X-Y coordinate space
    legend_handles(i) = plot(X_combined, Y_combined, '.');
% Store the handle of the plot

    % Add the current alpha value to the legend labels
    legend_labels{i} = ['? = ', num2str(rad2deg(alpha)), '
°'];

    %plotting the rigid arms
    xp=linspace(0,min(X_combined),100);
    yt=[];
    for ii =1:length(xp)
        yp=tan(alpha+gamma)*xp(ii);
        yt=[yt,yp];
    end

    plot(xp,yt,'k', 'LineWidth', 3,
'HandleVisibility','off'); % Hide from legend
```

```
    x2=xp+max(X_combined);
    y2=fliplr(yt);
    plot(x2,y2,'k', 'LineWidth', 3,
'HandleVisibility','off'); % Hide from legend

    % Compute the curvature at the midpoint of the curve
    ds = beta_values(2) - beta_values(1); % step size
    mid_idx = round(length(beta_values)/2); % index of the
midpoint
    x_prime = (X_values(mid_idx+1) - X_values(mid_idx-1)) /
(2*ds);
    y_prime = (Y_values(mid_idx+1) - Y_values(mid_idx-1)) /
(2*ds);
    x_double_prime = (X_values(mid_idx+1) -
2*X_values(mid_idx) + X_values(mid_idx-1)) / (ds^2);
    y_double_prime = (Y_values(mid_idx+1) -
2*Y_values(mid_idx) + Y_values(mid_idx-1)) / (ds^2);
    kappa = abs(y_double_prime*x_prime -
y_prime*x_double_prime) / (x_prime^2 + y_prime^2)^(3/2);
    Kap = [Kap, kappa]; % store the curvature value
end

title('Elastica solutions for CBT');
xlabel('X (mm)');
ylabel('Y (mm)');
hold off
% Add the legend to the plot
legend(legend_handles, legend_labels); % Use the stored
handles for the legend

hold off
plot(D_X,Kap,'*');
hold on
plot(Delta_DIC{1,3}, K_DIC_M{1,3},'.')
hold on
plot(DeltaP{1,3}, K_Matrix{1,3},'.')
title('Delta vs Curvature for three solution methods')
xlabel('Delta(mm)');
ylabel('Curvature(1/mm)');
legend('Elastica solution','DIC readings', 'Closed form
solution')

%%
```

```
Elas_force = interp1(DeltaP{1,3}, Force_G{1,3}, D_X,
'linear', 'extrap');
Elas_Moment=Elas_force.*D_Y/20.33;

plot(Kap(5:end),Elas_Moment(5:end),'r','LineWidth',2.5);
hold on
K_geom=K_Matrix{1,3};
M_geom=M_Matrix{1,3};
plot(K_geom(290:end-150),M_geom(290:end-
150),'k','LineWidth',2.5);

%%
Elas_force = interp1(DeltaP{1,3}, Force_G{1,3}, D_X,
'linear', 'extrap');
Elas_Moment=Elas_force.*D_Y/20.27;

plot(Kap(5:end),Elas_Moment(5:end),'-k','LineWidth',2.5);
hold on
grid on
K_geom=K_Matrix{1,3};
M_geom=M_Matrix{1,3};
K_geom=K_geom(290:end-150);
M_geom=M_geom(290:end-150);
% Create a common K vector with 0.01 intervals
K_common = min(K_geom):0.01:max(K_geom);

% Interpolate the M values at the K_common values
M_interp = interp1(K_geom, M_geom, K_common, 'linear',
'extrap');

% Plot the interpolated M values against the common K
values
plot(K_common, M_interp, '-s','MarkerSize',10,...
    'MarkerEdgeColor','black',...
    'MarkerFaceColor',[1 .6 .6]);
```

DIC analysis of the column bending test

```
%% Data from DIC

    filename_DIC = ['CBTD90_C22_F_SP' num2str(i) '.csv'];
    filepath = fullfile(folder1, filename);
    time_0 = xlsread(filename_DIC, 'B:B');
    time_1 = xlsread(filename_DIC, 'C:C');
    r_DIC_Avg = xlsread(filename_DIC, 'I:I')-4.7 ;
    K_DIC_Avg = xlsread(filename_DIC, 'N:N').*(-2);
    r_DIC_R0 = xlsread(filename_DIC, 'X:X') -4.7;
    K_DIC_R0 = xlsread(filename_DIC, 'AC:AC').*(-2);
    avgtime = (time_0 + time_1)/2;
    time_DIC = avgtime - avgtime(1);
    time_DIC(time_DIC > time(end)) = [];
    ind = zeros(1,length(time_DIC));
    for t=1:length(time_DIC)
        ind_temp = find(abs(time - time_DIC(t)) < 0.02);
%check this: find a better way to do this
        if length(ind_temp) > 1
        %fprintf('%.0f indices found for i=%.0f, t=%.0f and
the minimum was selected\n',length(ind_temp),ii,t);
        [~,ind_temp] = min(abs(time - time_DIC(t)));
        end
    ind(t) = min(ind_temp);
    end
M_DIC = p(ind).*r_DIC_R0(1:length(ind))/w;
DeltaD=delta(ind);
K_DIC = K_DIC_R0(1:length(ind));
t_DIC = time(ind);
% D11 = diff(M_DIC)./diff(K_DIC);
% Adjsut origin
switch ii
    case 1
        % K_DIC = K_DIC - 0.045301 + 0.020554;
        K_DIC = K_DIC; %- 0.045301 + 0.027815 - 0.017962;
    case 2
        % K_DIC = K_DIC - 0.038848 + 0.015181;
        K_DIC = K_DIC; %- 0.038848 + 0.026492 -0.017739 +
0.0093354;
    case 3
        % K_DIC = K_DIC - 0.034802 + 0.016163;
```

```
        K_DIC = K_DIC; %- 0.034802 + 0.02157 - 0.025072 +
0.0074537;
    case 4
        % K_DIC = K_DIC - 0.036712 + 0.015438;
        K_DIC = K_DIC; %- 0.036712 + 0.022996 - 0.023119 +
0.011438;
    case 5
        K_DIC = K_DIC;
    case 6
        K_DIC = K_DIC;
    case 7
        K_DIC = K_DIC;
    case 8
        K_DIC = K_DIC;
    case 9
        K_DIC = K_DIC;
    case 10
        K_DIC = K_DIC;
    case 11
        K_DIC = K_DIC;
end

%material non-linearity

%     t=0.18;
%     Nl_M=[];
%     E1=233000*0.5; %fibre E1 property and volume fraction
for t300-1k
%     gamma=40;
%     for j=1:length(K)
%         Nl_M(j)=(1/72)*E1*K(j)*(t^3)*((36-
3*(t^2)*(gamma^2)*(K(j)^2))^0.5);
%     end
%
%     Nl_M=transpose(Nl_M);
%     plot(K_DIC,M_DIC,'b',K, M, 'r');


  K_DIC_M{end+1}=K_DIC;
  M_DIC_M{end+1}=M_DIC;
  Delta_DIC{end+1}=DeltaD;

end
```

Curve fitting of the DIC plots

```
%DIC K vs M plots without reducing 4.7 from the moment
arms(4th deg fits)

P1 = [-1688; -1.731e+04; -2027; 842.1; 84.94; -3206; -2170;
-8662; -1.012e+04; -1.018e+04; -3017];
P2 = [684.9; 5608; 1132; -284.5; -71.36; 1734; 1101; 3345;
3628; 3759; 1305];
P3 = [-150.9; -715.6; -271; 59.89; 35.25; -374.7; -243.7; -
515.5; -521.1; -540.3; -252.2];
P4 = [41.87; 72.86; 49.36; -0.5973; -0.2044; 63.35; 50.09;
66.24; 64.5; 63.78; 43.6];
P5 = [-0.4225; -0.7351; -0.3791; NaN; NaN;-0.802; -0.461; -
0.6291; -0.6528; -0.409; -0.3806];
Poly = [4; 4; 4; 3; 3; 4; 4; 4; 4; 4; 4];
figure;
hold on
all_dy_dx = [];
for i=1:11

  if (i ~= 4 && i ~= 5  )
    K=cell2mat(K_DIC_MN(i));
    if (i==4 && i==5 )
        M=cell2mat(M_DIC_MN(i))-P4(i);
    else
        M=cell2mat(M_DIC_MN(i))-P5(i);
    end

    [UBM,id]=max(M);
    UBK=K(id);

    x=linspace(0,UBK,1000);
    p11=P1(i);
    p22=P2(i);
    p33=P3(i);
    if ( i==4 || i==5 )
        fun=@(x) p11 *x^3 +p22*x^2+p33*x+0;
    else
        p44=P4(i);
        fun=@(x) p11*x^4+p22 *x^3 +p33*x^2+p44*x+0;
    end
```

```
    y=[];
    ii=0;

    for ii = x
        yi=fun(ii);
        y=[y, yi];
    end


%   Plot the parabola and data points
%     plot(x, y);
    dy_dx = gradient(y, x);
    all_dy_dx = [all_dy_dx; dy_dx];
    plot(x, dy_dx,'LineWidth', 1.5);
%     plot(K, M, '.', 'MarkerSize', 5);
%     legend('DIC');
    grid on;
    box on;

    % Create legend for current specimen (without K, M
plot)
%     legendStr = sprintf('Specimen-%d', i);
%     legend(legendStr);

  end
end
%
% % Plot vertical lines
% for i = 1:11
%     if (i == 1 || i == 3 || i == 4 || i == 5 || i == 6 ||
i == 7 || i == 8 || i == 9 || i == 10 || i == 11)
%         K = cell2mat(K_DIC_M(i));
%         M = cell2mat(M_DIC_M(i)) - p33(i);
%         [~, id] = max(M);
%         UBK = K(id);
%         maxM = max(M);
%         plot([UBK UBK], [maxM maxM - 0.5], 'k--');
%     end
% end
%
mean_dy_dx = mean(all_dy_dx, 1);
std_dy_dx = std(all_dy_dx, 0, 1);
plot(x, mean_dy_dx, 'LineWidth', 2.5);
```

```
hold on;
fill([x, fliplr(x)], [mean_dy_dx-std_dy_dx,
fliplr(mean_dy_dx+std_dy_dx)], 'r', 'FaceAlpha', 0.1,
'EdgeColor', 'none');
% plot(Curve1,MatOri,'LineWidth', 2.5 );
% plot(Curve1,Dry,'LineWidth', 2.5 );
hold on
% plot(Curve1, failure, 'rx', 'MarkerSize', 10);
% legend('Dry fibre model', 'Mat Ori model', 'Failure
points');
hold off
% xlabel('Curvature');
% ylabel('Moment');
title('4th degree fitting without reducing 4.7');

% % Legends for Dry, MatOri, and failure points
```

UGENS subroutine for non-linear section stiffness variation

```
       SUBROUTINE
UGENS(ddndde,force,statev,sse,spd,pnewdt,stran,dstran,
     &
tss,time,dtime,temp,dtemp,predef,dpred,cename,ndi,nshr,nsecv,
     &
nstatv,props,jprops,nprops,njprop,coords,celent,thick,dfgrd,curv
,
     & basis,noel,npt,kstep,kinc,kit,linper)

      include 'aba_param.inc'

      character*80 cename
      dimension force(nsecv),statev(nstatv),ddndde(nsecv,nsecv),
     & stran(nsecv),dstran(nsecv),predef(*),dpred(*),
     & props(*),jprops(*),coords(3),time(2),dfgrd(3,3),
     & curv(2,2),basis(3,3),tss(*)
      dimension MD11(100)
      dimension eD11(100)
       dimension D11STIF(87)
      dimension STIF(100,6,6),e(100,6,6)
      integer i,ii,j,jj,kk,m,k,n,current_Id,next_Id,ij,gg
      double precision e_int1,e_int2,stranCurrent,stranNext
      double precision A11nonl,A22nonl,k_nl
      parameter (zero=0.0d0,half=0.5d0)

 ! STRESS RESULTANT vs. STRAIN RELATIONS / RVE ANALYSIS --------
------------------------
 ! PRE-DEFINED CURVATURE POINTS
       eD11=(/1.0000e-02,1.2000e-02,1.3800e-02,1.5800e-
02,1.7700e-02,1.9600e-02,
     + 2.1500e-02,2.3400e-02,2.5400e-02,2.7300e-02,2.9200e-
02,3.1100e-02,
     + 3.3000e-02,3.4900e-02,3.6900e-02,3.8800e-02,4.0700e-
02,4.2600e-02,
     + 4.4500e-02,4.6500e-02,4.8400e-02,5.0300e-02,5.2200e-
02,5.4100e-02,
     + 5.6100e-02,5.8000e-02,5.9900e-02,6.1800e-02,6.3700e-
02,6.5700e-02,
     + 6.7600e-02,6.9500e-02,7.1400e-02,7.3300e-02,7.5300e-
02,7.7200e-02,
     + 7.9100e-02,8.1000e-02,8.2900e-02,8.4800e-02,8.6800e-
02,8.8700e-02,
```

```
     + 9.0600e-02,9.2500e-02,9.4400e-02,9.6400e-02,9.8300e-
02,1.0020e-01,
     + 1.0210e-01,1.0400e-01,1.0600e-01,1.0790e-01,1.0980e-
01,1.1170e-01,
     + 1.1360e-01,1.1560e-01,1.1750e-01,1.1940e-01,1.2130e-
01,1.2320e-01,
     + 1.2520e-01,1.2710e-01,1.2900e-01,1.3090e-01,1.3280e-
01,1.3470e-01,
     + 1.3670e-01,1.3860e-01,1.4050e-01,1.4240e-01,1.4430e-
01,1.4630e-01,
     + 1.4820e-01,1.5010e-01,1.5200e-01,1.5390e-01,1.5590e-
01,1.5780e-01,
     + 1.5970e-01,1.6160e-01,1.6350e-01,1.6550e-01,1.6740e-
01,1.6930e-01,
     + 1.7120e-01,1.7310e-01,1.7510e-01,1.7700e-01,1.7890e-
01,1.8080e-01,
     + 1.8270e-01,1.8460e-01,1.8660e-01,1.8850e-01,1.9040e-
01,1.9230e-01,
     + 1.9420e-01,1.9620e-01,1.9810e-01,2.0000e-01 /)

 ! CORRESPONDING MOMENTS
       MD11=(/3.0000e-01,3.7300e-01,4.3840e-01,5.0630e-
01,5.7400e-01,6.4140e-01,
     + 7.0850e-01,7.7540e-01,8.4190e-01,9.0820e-01,9.7420e-
01,1.0400e+00,
     +
1.1050e+00,1.1700e+00,1.2350e+00,1.2990e+00,1.3630e+00,1.4270e+0
0,
     +
1.4900e+00,1.5540e+00,1.6160e+00,1.6780e+00,1.7400e+00,1.8020e+0
0,
     +
1.8630e+00,1.9240e+00,1.9840e+00,2.0440e+00,2.1030e+00,2.1630e+0
0,
     +
2.2210e+00,2.2790e+00,2.3370e+00,2.3940e+00,2.4510e+00,2.5080e+0
0,
     +
2.5640e+00,2.6190e+00,2.6740e+00,2.7290e+00,2.7830e+00,2.8370e+0
0,
     +
2.8900e+00,2.9420e+00,2.9940e+00,3.0460e+00,3.0970e+00,3.1470e+0
0,
     +
3.1970e+00,3.2470e+00,3.2950e+00,3.3440e+00,3.3910e+00,3.4380e+0
0,
```

```
     +
3.4850e+00,3.5310e+00,3.5760e+00,3.6210e+00,3.6650e+00,3.7090e+0
0,
     +
3.7520e+00,3.7940e+00,3.8360e+00,3.8770e+00,3.9170e+00,3.9570e+0
0,
     +
3.9960e+00,4.0350e+00,4.0730e+00,4.1100e+00,4.1460e+00,4.1820e+0
0,
     +
4.2170e+00,4.2510e+00,4.2850e+00,4.3180e+00,4.3500e+00,4.3820e+0
0,
     +
4.4130e+00,4.4430e+00,4.4720e+00,4.5010e+00,4.5290e+00,4.5560e+0
0,
     +
4.5820e+00,4.6070e+00,4.6320e+00,4.6560e+00,4.6790e+00,4.7020e+0
0,
     +
4.7230e+00,4.7440e+00,4.7640e+00,4.7830e+00,4.8010e+00,4.8190e+0
0,
     + 4.8350e+00,4.8510e+00,4.8660e+00,4.8800e+00 /)

 ! State variable definition
      statev(1)=noel; statev(2)=npt; statev(3)=kstep;
statev(4)=kinc;
      statev(5)=kit; statev(6)=time(1);
statev(7)=dtime;statev(8)=thick;
      statev(9)=celent; statev(10)=temp; statev(11)=dtemp;
      statev(12)=zero; statev(13)=zero
      k3=0
      do k1=1,3
       do k2=1,3
        statev(14+k3)=basis(k1,k2)
        statev(23+k3)=dfgrd(k1,k2)
        k3=k3+1
       end do
      end do
      statev(32)=curv(1,1); statev(33)=curv(1,2);
statev(34)=curv(2,1)
      statev(35)=curv(2,2); statev(36)=tss(1); statev(37)=tss(2)
      statev(38)=coords(1); statev(39)=coords(2);
statev(40)=coords(3)
      do k1=1,nsecv
       statev(40+k1)=stran(k1)
      end do
       istatev=40+nsecv
```

```
! Jacobian definition
     ddndde(1,1) = props(1)
     ddndde(1,2) = props(2)
     ddndde(2,2) = props(3)
     ddndde(1,3) = props(4)
     ddndde(2,3) = props(5)
     ddndde(3,3) = props(6)
     ddndde(1,4) = props(7)
     ddndde(2,4) = props(8)
     ddndde(3,4) = props(9)
     ddndde(4,4) = props(10)
     ddndde(1,5) = props(11)
     ddndde(2,5) = props(12)
     ddndde(3,5) = props(13)
     ddndde(4,5) = props(14)
     ddndde(5,5) = props(15)
     ddndde(1,6) = props(16)
     ddndde(2,6) = props(17)
     ddndde(3,6) = props(18)
     ddndde(4,6) = props(19)
     ddndde(5,6) = props(20)
     ddndde(6,6) = props(21)

     do i=1,nsecv
      do j=1,i
        ddndde(i,j) = ddndde(j,i)
      end do
     end do

! initializing stiffness and strain arrays

     do ii=1,100
      do jj=1,6
       do kk=1,6
          STIF(ii,jj,kk)= 0
          e(ii,jj,kk)= 0
       end do
      end do
     end do

! ASSEMBLE STIFFNESS 3D ARRAY
     do m=2,100
      STIF(m-1,1,1) = 8.493e+03
       STIF(m-1,1,2) = 2.195e+03
       STIF(m-1,1,3) = 0
       STIF(m-1,1,4) = 0
```

```
         STIF(m-1,1,5) = 0
         STIF(m-1,1,6) = 0
         STIF(m-1,2,1) = 2.195e+03
         STIF(m-1,2,2) = 8.493e+03
         STIF(m-1,2,3) = 0
         STIF(m-1,2,4) = 0
         STIF(m-1,2,5) = 0
         STIF(m-1,2,6) = 0
         STIF(m-1,3,1) = 0
        STIF(m-1,3,2) = 0
        STIF(m-1,3,3) = 0.370e+03
        STIF(m-1,3,4) = 0
        STIF(m-1,3,5) = 0
        STIF(m-1,3,6) = 0
        STIF(m-1,4,1) = 0
        STIF(m-1,4,2) = 0
        STIF(m-1,4,3) = 0
        STIF(m-1,4,4) = 36.5
        STIF(m-1,4,6) = 0
        STIF(m-1,5,1) = 0
        STIF(m-1,5,2) = 0
         STIF(m-1,5,3) = 0
         STIF(m-1,5,4) = 0.470e+01
         STIF(m-1,5,5) = 36.5
         STIF(m-1,5,6) = 0
         STIF(m-1,6,1) = 0
         STIF(m-1,6,2) = 0
         STIF(m-1,6,3) = 0
         STIF(m-1,6,4) = 0
         STIF(m-1,6,5) = 0
         STIF(m-1,6,6) = 0.180e+01
       end do

      !stiffness array for D11 and D44

       D11STIF=(/ 35.83, 35.69, 35.54, 35.39, 35.24, 35.09,
34.93, 34.77,
     &       34.61, 34.44,34.28, 34.11, 33.93, 33.76, 33.58,
33.40, 33.21, 33.02,
     &       32.83, 32.64,32.45, 32.25, 32.05, 31.84, 31.63,
31.42, 31.21, 30.99,
     &       30.77, 30.55,30.33, 30.10, 29.87, 29.63, 29.40,
29.16, 28.91, 28.66,
     &       28.41, 28.16,27.91, 27.65, 27.38, 27.12, 26.85,
26.58, 26.30, 26.02,
     &       25.74, 25.45,25.16, 24.87, 24.58, 24.28, 23.98,
23.67, 23.36, 23.05,
```

```
     &       22.73, 22.41,22.09, 21.76, 21.43, 21.10, 20.76,
20.42, 20.08, 19.73,
     &       19.38, 19.02,18.66, 18.30, 17.93, 17.56, 17.19,
16.81, 16.43, 16.05,
     &       15.66, 15.27,14.87, 14.47, 14.07, 13.66, 13.25,
12.83, 12.41 /)


  !ASSEMBLE STRAIN 3D ARRAY

      do m=2,100
       e(m-1,4,4)=eD11(m)
       e(m-1,5,5)=eD11(m)
      end do

  !Finding the current strain IDs

      StranCurrent = abs(stran(5))  ! Set StranCurrent to the
fourth element of the stran array
      ii = 1  ! Initialize ii, assuming starting index is 1

      do
          if (StranCurrent == 0.0) then
              current_Id = 1
              exit  ! Exit the loop as we found our condition
          elseif (StranCurrent <= e(ii,4,4)) then
              current_Id = ii
              exit  ! Exit the loop once the correct condition
is met
          else
              ii = ii + 1
              if (ii > size(e,1)) then  ! Check if ii exceeds
the bounds of e
                  exit  ! If ii is out of bounds, exit to avoid
an error
              endif
          endif
      end do

       !write(*,*) 'DEBUG: Current ID:',
StranCurrent,e(current_Id,4,4),current_Id

      jj = 1  ! Initialize jj
      StranNext = stran(5) + dstran(5)  ! Calculate StranNext
based on the fourth elements of stran and dstran
      StranNext=abs(StranNext)
```

```
  !Finding the current strain IDs
      do
          if (StranNext <= e(jj,4,4)) then
              next_Id = jj
              exit  ! Exit the loop as the condition is met
          else
              jj = jj + 1
              if (jj > size(e,1)) then  ! Check if jj exceeds
the bounds of e
                  print *, "No valid index found within bounds."
                  exit  ! If jj is out of bounds, exit to avoid
an error
              endif
          endif
      end do



      n = next_Id - current_Id
      !write(*,*)'currStiff',STIF(current_Id,4,4)

      do i=1,6
       do j=1,6
          if (i == 4 .and. j==4 .or. i == 5 .and. j==5) then
              !if (n == 0) then
              force(i)=force(i)+D11STIF(current_Id)*dstran(j)

               !else if (n > 0) then
                 !e_int1 = e(current_Id, i, j) - stranCurrent
                 !e_int2 = stranNext - e(current_Id + n - 1, i,
j)
                 !force(i) = force(i) + D11STIF(current_Id) *
e_int1
                 !force(i) = force(i) + D11STIF(current_Id) *
e_int2
                 !do k = 2, n
                   !force(i) = force(i) + D11STIF(current_Id) *
     &          !(e(current_Id + k - 1, i, j) - e(current_Id + k
- 2, i, j))
              !end do
            !endif
           else
              force(i)=force(i)+STIF(1,i,j)*dstran(j)
         endif

       end do
       statev(istatev+i) = force(i)
```

```
       if (noel==90) then
           write(*,*) 'DEBUG:force and strain', force(5),
stran(5),kinc, noel
       endif
      end do
      RETURN
      END
```